Study of gas-sheared liquid film in horizontal rectangular duct using high-speed LIF technique: three-dimensional wavy structure and its relation to liquid entrainment.

Andrey V. Cherdantsev[1,2*], David B. Hann[1], Barry J. Azzopardi[1]

[1]University of Nottingham, Nottingham, United Kingdom
[2]Kutateladze Institute of Thermophysics, Novosibirsk, Russia

*corresponding author, e-mail: cherdantsev@itp.nsc.ru

Keywords: gas-sheared liquid film; disturbance waves; ripples; liquid entrainment; annular flow; laser-induced fluorescence.

Abstract

The flow of a liquid film sheared by high velocity gas stream in a horizontal rectangular duct was investigated using a high-speed laser-induced fluorescence technique. Measurements of local film thickness were resolved in both longitudinal and transverse coordinates with high spatial and temporal resolution. It was found that the generation of fast and slow ripples by the disturbance waves was qualitatively the same as it was observed earlier in completely different conditions. The transverse size and curvature of the disturbance waves and ripples were measured. A relationship between the three-dimensional structure of ripples on top of disturbance waves and the two mechanisms of liquid entrainment, known as 'bag break-up' and 'ligament break-up', is proposed.

1. Introduction

The simultaneous flow of a liquid film and high-velocity gas stream occurs in a variety of industrial equipment. Due to variations in the gas shear stress and pressure along the film, complex wavy structures can appear on the film surface. Large-scale disturbance waves, separated by relatively thin base film layer, dominate this situation. Small-scale ripple waves can coexist with disturbance waves, travelling either over the waves or over the base film. Liquid droplets can be torn from film surface and entrained into the core of gas stream. The presence of waves and entrainment exerts a very significant influence on the integral flow characteristics such as pressure drop and heat transfer.

The prediction of the integral characteristics of the gas-sheared film flow is a well-known challenge. Two approaches are used to overcome this. The first approach is to measure the integral characteristics and correlate the obtained values to the inlet gas and liquid flow rates, average film thickness and other flow parameters. This approach is widely used, and numerous empirical correlations with limited applicability have been developed. The second approach is to develop physically-based models based on direct experimental observations of how the droplets are torn from film surface and experimental studying of the wavy structure.

A number of very varied techniques have been employed to visualize entrainment. Woodmansee & Hanratty (1969) performed high-speed photography of film surface in a horizontal rectangular duct, with the camera looking from below. They observed that the ripples travelling over disturbance waves can be accelerated and scattered into droplets. Azzopardi (1983) studied the entrainment in upward vertical flow in a pipe using camera looking along the axis of the pipe. It was observed that droplets are ejected from wave structures via formation of transitional liquid structures of two kinds, called 'liquid bags' and 'liquid ligaments'. Pham et al. (2014) studied the gas-sheared liquid film on the outer surface of a vertical cylinder, part of a rod bundle. Because of their geometry, they were able to observe the entrainment from the side. They also found that the tiny waves on top of larger disturbance waves are deformed and scattered via bag and ligament break-up mechanisms. The formation of drops by depositing drops was also found to be significant.

Disturbance waves have been investigated in a large number of papers. Most of these papers were devoted to measuring the average characteristics of disturbance waves such as velocity, frequency, amplitude, longitudinal size, etc (see, e.g., Chu and Dukler 1975; Azzopardi 1986; Han et al. 2006; Sawant et al. 2008). From these papers it was found that: velocity and frequency of disturbance waves grow linearly with increasing gas velocity, wave amplitudes decrease with gas velocity, longitudinal size of disturbance waves tends to be constant at different gas velocities, and increase in liquid flow rate leads to increase in all the mentioned quantities. As a rule, such measurements were performed far from the inlet where the flow is considered to be fully developed.

It was also shown that disturbance waves are formed near the inlet and individual disturbance waves were found to travel with nearly constant velocity over large distances (Hall Taylor et al. 1963). Nonetheless, the velocity of individual disturbance waves may be different in the same flow conditions. When a faster wave overtakes a slower one, a new wave is formed with velocity close to that of the faster wave. Coalescence will cause the frequency of disturbance waves to decrease with downstream distance.

The transverse structure of disturbance waves has been mainly studied in pipes. In this configuration it was found that disturbance waves in small diameter (lesser than 30 mm) pipes form full rings around the circumference of the pipe, while in larger diameter pipes, circumferentially localized disturbance waves appear (Azzopardi, 1997). The height of the disturbance waves was found to be non-uniform in the circumferential direction (Belt et al. 2010), and Zhao et al. (2013) observed that the circumferential coherence of disturbance waves increases downstream.

Until recently, ripples were rarely studied due to the low spatial resolution of most measurement techniques employed. An exception is the work of Chu & Dukler (1974), where the main properties of ripples on the base film were measured. With recent development of high-resolution techniques (in particular, planar laser-induced fluorescence), more detailed investigation of ripples has become possible. Schubring et al. (2010) used PLIF technique to measure the amplitudes of ripples on the base film and on disturbance waves separately. They generated simple relationships between the ripples' amplitude and the average film thickness in the base film and disturbance waves regions.

Alekseenko et al. (2009) employed a laser-induced fluorescence (LIF) technique to perform high-speed field measurements of film thickness, and, hence, study the temporal and spatial evolution of all the waves simultaneously. This technique was applied for downward annular flow in 15 mm pipe, where it was found that all the ripples are generated at the back slopes of disturbance waves, and they can move either faster or slower than 'parent' disturbance waves. Slow ripples travel over the base film, and fast ripples travel over disturbance waves, disappearing near the fronts of disturbance waves. It was suggested that the disappearance occurs due to disruption of fast ripples by the gas shear into droplets that are entrained into the gas core.

In the present work, a LIF technique is applied for investigation of gas-sheared film flow in horizontal rectangular duct. The technique makes it possible to perform field measurements of local film thickness, resolved in both space and time, similar to the work of Alekseenko et al. (2009). The flat shape and large transverse size of the duct allow us to resolve the film thickness in transverse coordinate as well. Alekseenko et al. (2012) attempted to do this in annular downward flow, but, for technical reasons, the sampling frequency was not high enough in their experiments. More recently Alekseenko et al. (2014a) showed that the LIF technique can also detect entrained droplets. The technique allows the simultaneous study of three-dimensional wavy structures and liquid entrainment, and can improve understanding of the entrainment phenomenon.

2. Description of experiments

2.1. Experimental setup and flow conditions

The experiments were conducted in a horizontal transparent acrylic resin duct with rectangular cross-section, as shown in Fig. 1. The length of the duct was 2 m; the width, W, was 161.4 mm and height, H, was 25 mm. The hydraulic diameter of the duct, D_h, was 43.3 mm. During the experiments, liquid was pumped continuously from the receiving tank, returning either through working section or through the bypass line. The liquid flow rate was controlled by a system of variable area flow meter. Air was supplied by a 15 kW blower, and the flow rate was measured by an orifice plate monitored by a digital manometer. The inlet of working section was divided into two parts separated by a horizontal plate located 3 mm above the duct bottom. Liquid was introduced through the lower slot; air through the upper slot. The temperatures of liquid and gas were measured by thermocouples upstream the inlet. The water temperature was 18-21°C and the air temperature was 35-40°C, due to the effect of the blower. The temperatures were stable during long-time runs.

The gas superficial velocity V_g was varied in the range 16-35 m/s and the liquid Reynolds number Re_L was varied within the range 155 to 520. Re_L was defined as $q/W\nu$, where q is volumetric liquid flow rate and ν is kinematic viscosity of liquid. Tap water containing Rhodamine 6G at a concentration of 15 mg/litre was employed as working liquid. Measurements were made at a distance 1.60 m ($37D_h$) downstream of the inlet.

2.2. Measurements technique

Measurements were performed using a laser-induced fluorescence technique. The technique is very similar to that used by Alekseenko et al. (2012), but with some minor differences. The main one is that a high-energy pulse laser (527 nm 15 mJ Nd:YLF laser) was used for fluorescence excitation instead of continuous one. This gave much better illumination, providing possibility to obtain data at a high repetition rate of up to 10 kHz. In addition, the real exposure time in present experiments was defined by duration of laser pulse, i.e., 100 ns. This time is much smaller than characteristic time of hydrodynamic processes in the flow; thus, the exposure blurring was negligible.

The laser beam was either converted into narrow optical sheet or spread over large area using scattering lens (see below). The relative brightness of fluorescent light was measured by

Phantom camera, synchronized with the laser pulse. Both camera and laser were placed below the bottom of the duct as close as possible to each other.

The measured brightness $J(x,y)$ depends on the local film thickness $h(x,y)$ obeying the relation:

$$\frac{J(x,y)-D(x,y)}{C(x,y)} = [1-e^{-\alpha \cdot h(x,y)}] \cdot [1+k_{refl} \cdot e^{-\alpha \cdot h(x,y)}] \quad (1)$$

The components making up equation (1) are:

- α, the coefficient of light absorption by fluorescent matter. It was quantified by comparing brightness of liquid in two slots of known thickness.
- k_{refl} is the reflection coefficient at liquid-gas interface, which is equal 0.02.
- $D(x,y)$ is the dark level of camera. It was measured when camera lens was closed.
- $C(x,y)$ is the compensation matrix. It was constructed in order to compensate non-uniformity of local illumination of the area of measurements by the laser light. For this, time-averaged local brightness $J_{ref}(x,y)$ was measured during long-time run under certain experimental conditions (namely, V_g=16 m/s and Re_L=220). It was assumed that $J_{ref}(x,y)$ corresponds to the average value of film thickness $<h>$ at these flow parameters.
- $<h>$ value was obtained independently using laser focus displacement (LFD) sensor, produced by Keyence co., Japan. The detailed description of the LFD technique applied for film thickness measurements can be found in, e.g., Takamasa & Hazuku (2000). The technique was applied in present experimental setup by Alghoul (2011). At V_g=16 m/s and Re_L=220 $<h>$ is equal 0.4 mm.

For each pair (x,y) the equation (1) can be transformed into a quadratic equation for $\exp(-\alpha h)$. After that, h(x,y) is expressed as natural logarithm of the positive root of this equation, divided by $(-\alpha)$.

2.3. Configurations of interrogation area

Three different configurations of interrogation area were used in present experiments. The first one was used for the purpose of comparison to the earlier data, in particular, to check whether the qualitative behavior of disturbance waves and fast and slow ripples corresponds to the behavior described by Alekseenko et al. (2009). These experiments were conducted in a similar manner: a laser sheet was oriented along one central longitudinal section of the rig. The area of 1280*1 pixel was investigated with spatial resolution 0.1 mm per pixel.

In the second case, transverse section of the duct was illuminated by a transversely-oriented laser sheet, covering the whole width of duct. Size of working area in pixels was also 1*1280, with spatial resolution 0.125 mm per pixel. The aim of this configuration was to investigate the transverse non-uniformity of disturbance waves.

In the third case, the laser beam was not converted into the optical sheet but was scattered over a large area using a scattering lens. A rectangular area 100 mm long and 50 mm wide was used as the area of interrogation. Spatial resolution was 0.1 mm per pixel. The third case was aimed to study the structure of fast ripples on disturbance waves and to study the process of liquid entrainment from film surface.

3. Results: Wavy structure

3.1. Waves dynamics in *t-x* representation

The first set of experiments was conducted with single line of camera pixels aimed to the central longitudinal section of the duct. Figure 2a presents fragment of film thickness matrix *h(t,x)* which shows temporal and spatial evolution of liquid film in this area. Size of the fragment is 100 mm by 100 ms; local brightness of image is directly proportional to local film thickness. Each string of this matrix is an instantaneous profile of film thickness along investigated section of the rig. Each column of this matrix is a temporal record of film thickness at fixed longitudinal distance.

The disturbance wave is seen in this fragment as wide brighter band, crossing the image from left to right. The slope of the trajectory of the disturbance wave relative to the *t*-axis is proportional to its velocity, which is constant within the area of measurements. The base film outside disturbance wave is covered by low-amplitude slow ripples (marked by 1 in Fig. 2), which are generated at the back slope of the disturbance wave. Slow ripples decelerate in time and travel over the base film behind parent disturbance wave until the following disturbance wave absorbs them. The surface of the disturbance wave is covered by high-amplitude fast ripples (marked by 2), which also appear at the back slope of the disturbance wave. Fast ripples travel faster than parent disturbance wave; when they reach front of disturbance wave, they disappear. Besides fast and slow ripples, two more types of structures can be seen in Fig. 2, namely, water droplets, entrained from film surface (marked as 3) and air bubbles, entrapped in liquid film (marked as 4). The former look like short bright streaks with high slope to *t*-axis; the latter look like dark lines with bright edges; their velocity doesn't exceed velocity of nearby ripples. Another example image with larger scale is shown

in Fig. 2b.

The described spatio-temporal behavior of disturbance waves and ripples is exactly the same as that observed by Alekseenko et al. (2009) for downward annular flow in vertical 15 mm i.d. pipe. This supports the idea of universal structure of disturbance waves and scenario of ripples' generation independent on shape, size and orientation of a duct.

Despite qualitative similarity of spatio-temporal behavior of disturbance waves and ripples in different conditions, there exist numerous quantitative differences. The most obvious differences are related to properties of disturbance waves. Fig. 3 shows comparison of such properties between present experiments and results of Alekseenko et al. (2014b). The latter results are obtained for air-water downward flow in 11.7 mm internal diameter pipe at the distance of 41 pipe diameters below the inlet. Data are presented for average velocity (Fig. 3a) and passing frequency (Fig. 3b) of disturbance waves. The average velocity was obtained by cross-correlating the temporal records of film thickness at two downstream distances. The frequency was measured by direct counting the space-time trajectories of individual disturbance waves. Average velocity of disturbance waves in downward annular flow is 1.5-2 times larger than that in horizontal rectangular duct. We suppose that this difference in mainly explained by flow orientation, since in the downward flow gravity contributes to the velocity of waves. The average velocity of large waves on liquid films falling under action of gravity in absence of gas flow is about 1.3-1.5 m/s for used range of liquid Reynolds numbers (see, e.g., Chu & Dukler 1975). Passing frequency in present experiments is also much smaller than that in vertical flow in narrow pipe. This difference can mainly be explained by the difference in equivalent diameters of the ducts. According to the empirical correlation, used in a large number of papers (see, e.g., Alamu & Azzopardi 2011), the frequency of waves decreases with pipe diameter. Average film thickness is also larger in present experiments; this is consistent with observed lower velocity of the film in this case. Since the film is not accelerated by gravity, it should be thicker for the same liquid flow rate.

An essential limitation of the brightness-based LIF technique consists in presence of optical distortions that cause sharp non-physical peaks to appear in the film thickness records. Such peaks are localized at steep slopes of liquid surface, namely, at front slopes of fast ripples and around the air bubbles entrapped by liquid film. Most likely, these peaks appear due to total internal reflection of exciting laser light on a steep liquid-gas surface. Example of such distortions is given in Fig. 4 is form of $h(x)$ in a fixed moment of time. In this Figure, two disturbance waves are present; one of them is between 0 and 20 mm, and the second is between 20 and 50 mm. It is impossible to wholly eliminate such distortions in the LIF data;

though, it is likely that they can be filtered off after thorough analysis, which can be done in future.

Outside the fast ripples, the film thickness data are reliable, and they can be used for identification of waves in LIF data. The present paper is focused on three-dimensional structure of the disturbance waves and fast ripples and their relation to entrainment.

3.2. Waves dynamics in *y-t* representation

To investigate the transverse structure of disturbance waves, experiments were conducted with laser sheet in a transverse orientation. A single transverse section of the duct was used as the area of interrogation. The camera obtained instantaneous distributions of film thickness over this section at 1280 points simultaneously, which gave spatial resolution of 0.125 mm. Such distributions were obtained with the same frame rate of 10 kHz.

Figure 5 shows examples of data in *y-t* representation. Each fragment has a spatial size of 161 mm (vertical axis) and duration of 400 ms (horizontal axis). Disturbance waves can be easily detected in these data as transversely oriented stripes of larger thickness. The average transverse size of the disturbance waves is definitely smaller than the rig width. Some waves occupy the whole width of the duct, whereas other waves are localized by the transverse coordinate. Narrower disturbance waves can either move along one of the side walls, or be localized in the center of the duct. This observation is consistent with earlier studies of circumferential coherence of disturbance waves in pipes of different diameters. Indeed, in small diameter pipe the localized disturbance waves are likely to close their edges and form a full ring around the pipe circumference, and in larger pipes they would remain localized. If we imagine that the bottom of the investigated duct is folded into a circular pipe, it would give a pipe with d=51 mm. In this case part of disturbance waves would form full rings, and the other part would be localized.

As a rule, the fronts of disturbance waves are horseshoe-shaped, with edges moving behind the central part of the wave. This shape can be described by a parabolic dependence of t (or x) on y. Film thickness behind the disturbance waves is not uniform. Edges of disturbance waves are followed by longitudinally oriented ‘tails’ of larger film thickness (marked as (1) in Fig. 5a), whereas the areas of reduced film thickness follow the central part of disturbance wave (marked as (2) in Fig. 5a). Though, sometimes localized tails of larger thickness appear behind the central part of the wave (marked as (3) in Figs. 5 b and c).

To investigate the transverse size and shape of disturbance waves, a simple threshold technique was used. The contours of disturbance waves were identified as lines where surface

h(y,t) crossed threshold value, equal to twice the thickness of the base film. To avoid splitting of contours, film thickness matrices were smoothed using running-average filter with width of averaging window 1.5 mm. Then the average coordinate of the contour was defined for each *y* position; obtained coordinates were approximated by parabolic dependence *t(y)*. Longitudinal 'tails' behind the edges of disturbance waves were not processed as part of disturbance wave and didn't contribute to the approximation.

The widths of the disturbance waves were defined as the transverse size of the contour. To characterize the curvature of disturbance waves, *t* was transformed into *x* using the cross-correlation velocity of disturbance waves, obtained in *t-x* representation at the previous stage (see subsection 3.1). Such transform introduces some uncertainty, since the velocity of individual disturbance waves may vary, as well as the velocity of different parts of disturbance waves. But it is the best way to estimate the longitudinal distortion of shape of disturbance waves at the present state of experiments.

The curvature was defined as second-order polynomial coefficient in parabolic approximation of a disturbance wave, with both *x* and *y* values given in millimeters. Physical sense of the curvature value can be understood as follows. Consider *x(y)* is the parabolic approximation of a wave's profile in *x-y* surface with the central point of the wave $\{x_0,y_0\}$. Thus, e.g., curvature value a_{dw}=0.05 denotes that at the transverse distance $y\text{-}y_0=1/a_{dw}$=20 mm, local longitudinal position of wave $x(y)\text{-}x_0$ will be also 20 mm.

Figure 6 correlates the widths and curvatures of all individual disturbance waves detected in *y-t* records with duration of 1 second for 8 regime points (Re_L=220 and Re_L=360, gas velocities in the range from 20 to 35 m/s). It can be seen that the waves, occupying the whole width of the duct, exist in the whole range of gas velocities. Waves with smaller width are more likely to appear at larger gas velocities. This result is consistent with results of Okada et al. (1995), who reported that the fraction of circumferentially localized disturbance waves in pipes increases with gas velocity. It can be also noted that the curvature of wide waves is always rather small, but the fronts of the narrow waves may be much more curved.

The simultaneous presence of waves of different scales suggests that the distribution of waves by their transverse size changes with downstream distance. Changes of scale might occur either due to fragmentation of wide waves into several narrow waves, or, vice versa, due to coalescence of narrow disturbance waves into the wider waves. It is impossible to identify which one of the two mechanisms is real, using the *y-t* representation of data. To answer this question, measurements of film thickness resolved in all three coordinates (*x*, *y* and *t*) are required.

3.3. Three-dimensional structure of disturbance waves

To study the three-dimensional wavy structure in dynamics, an area of interrogation with longitudinal size of 100 mm and width of 50 mm was used. At each time instant a matrix of film thickness values in this area was obtained with spatial resolution of 0.1 mm.

With this way of data representation it is possible to find out, whether coalescence or fragmentation of disturbance waves actually takes place. Figure 7 shows a sequence of frames, showing the instantaneous distribution of film thickness within the area of interrogation. Flow direction is from left to right. In the first frame edges of two localized disturbance waves are seen in the left part of the frame. The rear wave propagates with larger velocity and overtakes the other wave. After this, the edges of the two waves coalesce and form the central part of a new wave. The new wave is definitely wider and its front in the central part (visible in the area of interest) is nearly flat. The latter denotes essential decrease in the curvature due to coalescence.

Possibly, the coalescence is enhanced by the fact that the left edge of the rear wave is propagating over the high-thickness tail behind the right edge of the other wave, which might yield acceleration of the left edge of the rear disturbance wave. It is interesting that the tails behind the edges of disturbance wave still exist for some time after the coalescence. This could explain the longitudinal tails that are sometimes observed behind the central parts of disturbance waves. In this case, such tails are a kind of 'atavism' conserved in process of waves' evolution.

The full video of disturbance waves' coalescence shown in Fig. 7 is presented in supplementary video 1.

Therefore, the dynamics of the system of disturbance waves is expected to behave as follows. Initial disturbance waves that are formed not far from the inlet are localized by transverse coordinate and have high curvature. Due to variation in the velocity of individual disturbance waves, faster waves overtake the slower ones. If the transverse positions of waves are not much different, the standard scenario of coalescence is expected, which leads to formation of a wave with the same characteristics as that of the faster wave (see Hall Taylor et al. 1963, Wilkes et al. 1983). If the waves are separated by large transverse distance, they are expected to 'ignore' each other. But if the transverse distance between the edges of two waves is small, they form a new wave with larger transverse size and smaller curvature.

Fragmentation events were not observed in this data, however this might be due to the relatively small size of the area of measurements and relatively short duration of records.

Further studies might show the existence of fragmentation events if longer capture times were used since it is possible that both coalescence and fragmentation might occur in the same conditions. As an example, events of both types occur for three-dimensional waves on films falling in absence of gas flow (Adomeit & Renz 2000, Demekhin et al. 2007). Falling films have some similarity to the gas-sheared films in a number of aspects; one could expect that the similarity includes existence of fragmentation events as well.

Nonetheless, available experimental data show that gas-sheared and falling films are not wholly similar. Studying the gas-sheared films in pipes, Zhao et al. (2013) have found that the correlation between film thickness records obtained at different circumferential positions of a pipe increases with downstream distance. In other words, the degree of two-dimensionality of disturbance waves increases downstream when the gas shear is imposed. This indicates that the fragmentation is at least rarer event than the coalescence. Clark et al. (2001) compared the three-dimensional wavy structure for vertical falling film with and without co-current gas flow. They observed that in presence of gas flow the waves are essentially more two-dimensional than in absence of gas flow. We suppose that presence of gas flow exerts stabilizing influence on the waves, suppressing the transverse instability and preventing fragmentation.

Larger fractions of narrow curved disturbance waves at larger gas velocities (see Okada et al. 1995 and the present results) may seem to contradict to the analysis given above; nonetheless, it can be explained as follows. Consider the two waves with velocities V_i and V_j, generated with time interval dt_{ij}, with transverse distance between their edges suitable for coalescence. The distance at which these disturbance waves would coalescence and form a wider wave is expressed as:

$$xc_{ij} = \frac{V_i V_j}{V_i - V_j} dt_{ij}$$

The term V_iV_j is proportional to the squared average velocity of disturbance waves, which, in turn, is proportional to the squared superficial gas velocity V_g^2 (see Fig. 3a). V_i-V_j is proportional to the standard deviation of disturbance waves by velocity, σV. According to Hall Taylor & Nedderman (1968), this quantity does not show any strong dependence on V_g. And the average value of dt_{ij} is inversely proportional to the passing frequency of disturbance waves, f, which is proportional to V_g (see Fig. 3b). Thus, the average distance required for coalescence is expected to linearly grow with V_g.

$$< xc >= \frac{< V_i V_j >}{< V_i - V_j >} < dt_{ij} > \sim \frac{< V >^2}{\sigma V} \frac{1}{f} \sim V_g{}^2 \frac{1}{V_g} \sim V_g$$

In addition, the average transverse size of the initial disturbance waves is expected to decrease with V_g. This means that the probability for the two waves to be placed at the transverse distance required for edge coalescence would decrease with gas velocity as well.

3.4. Three-dimensional structure of fast ripples

Fast ripples on disturbance waves and slow ripples on the base film are also transversely localized and have curved fronts. It can be seen that the fast ripples are placed in staggered order, reminding the pattern of fish scales (Fig. 7). Unfortunately, the real placement of the fast ripples is essentially less regular than that of the fish scales. Fast ripples go in several layers, which are placed in staggered order. The number of layers is expected to be defined by the length of the disturbance wave. The neighboring fast ripples are placed close to each other. At the junction of two neighboring fast ripples, edges of ripples form longitudinally oriented 'crest', supported from behind by the central part of a ripple from the next layer (see 1 in Fig. 8a).

An example of passage of a single disturbance wave across the area of measurement is presented in supplementary video 2.

Since the fast ripples are expected to be related to liquid entrainment, quantitative investigation of their properties is the object of high scientific and practical interest. As mentioned above, local film thickness at the fronts of fast ripples is overestimated due to total internal reflection under high-slope liquid-gas interface. This gives extremely bright contours of fast ripples in *x-y* surfaces. Such contours help to identify the fast ripples visually. Though, the contours are difficult to use for automatic identification of fast ripples because of their irregularity, which appears due to minor variations of slope of a fast ripple's front. It is also complicated to eliminate these non-physical values of film thickness in order to process the real amplitude characteristics of the fast ripples. This problem requires additional considerations and, possibly, can be solved in future. At present, manual data processing was performed as follows.

The frames with disturbance waves, covering the whole width of the area of interrogation, were selected manually. For each disturbance wave 2-3 frames at different downstream distances were processed. For each frame, a visual search of individual fast ripples was performed. For each ripple, 4 points were marked; two of them corresponded to left and right edges of the ripple and the other two were placed around the central part of the ripple's front. The four points were then approximated by a parabolic line. Examples of such lines are shown in Fig. 8 by solid black lines. After all ripples on one frame were processed, the frame,

obtained 1 ms later, was processed in the same manner. This gave us possibility to repeat marking the front of each ripple, and to measure the velocities of individual ripples, based on the shift between the two contours. As the result, velocity, width and curvature of each ripple were recorded. Between 50 and 350 individual fast ripples were processed per regime point.

The results of these measurements are presented in Fig. 9. The average velocity of the fast ripples V_{fr} shows the same behavior with flow parameters as the velocity of disturbance waves (Fig. 9a). It is growing linearly with gas velocity and weakly grows with liquid Reynolds number. On average, fast ripples are 20-30% faster than the disturbance waves. The width (or transverse size) of fast ripples W_{fr} decreases with the gas velocity. Within our range of gas velocities it decreases 1.5-2 times, from 9-10 mm at Vg=20 m/s to 5-6 mm at Vg=35 m/s (Fig. 9b). The influence of liquid flow rate on ripples' width is much weaker. The average curvature of the fast ripples a_{fr} grows with gas velocity and also weakly grows with the liquid flow rate (Fig. 9c). As it could be expected, the curvature is much larger than that of disturbance waves. Fig. 9d shows the average longitudinal size of ripples L_{fr}. This quantity shows similar behavior to that W_{fr}, but the rate of decrease with gas velocity is smaller, which is consistent with the growth of curvature.

The scatter of the properties of the ripples is rather large. The standard deviation of the distribution of ripples with velocity for given regime point is in average around 25% of the average velocity of ripples. For the width of the ripples this value is about 20%, whilst for curvature it is more than 40%.

4. Droplet entrainment and its relation to the wavy structure

Though the experimental technique was originally developed for measurements of film thickness, different objects such as droplets entrained from film surface and bubbles entrapped inside the film are visible in the film thickness images as well. Droplets look like small bright areas travelling much faster than the waves. Individual droplets can be easily distinguished when studying the evolution of the field of film thickness obtained. Thus, it is possible to observe the entrainment process beginning from a certain stage, when droplets are already separated from the waves; moreover, it is possible to link the act of droplets creation with the elements of wavy structure of liquid film.

According to our observations, three different mechanisms of droplets creation exist in adiabatic flow of gas-sheared film. One of those mechanisms is the secondary entrainment due to impacts of droplets onto film surface. This mechanism is not directly related to the wavy structure of liquid film and will not be regarded in details in the present paper. The

other two mechanisms are exactly the ‘bag break-up’ and ‘ligament break-up’ mechanisms, identified for the first time by Azzopardi (1983) and observed recently by Lecoeur et al. (2010) and Pham et al. (2014). Both mechanisms link the droplet entrainment to the disruption of fast ripples on disturbance waves by the gas shear. In the two cases, different liquid structures are created due to deformation of different elements of film surface. Examples of frame sequences, showing bag and ligament break-up modes for different flow regimes are presented in Figures 10 and 11, respectively.

In case of bag break-up an arc of liquid appears in front of disturbance wave (Fig. 10). The arc protrudes forward and expands until it is being broken into a number of small droplets. According to earlier observations, the bag consists of thin deformed liquid sheet surrounded by thicker rim. The liquid sheet is broken first into a number of very small droplets; then the rim is broken into larger droplets. Thus, what we can see is actually the rim’s evolution and disruption. Full videos of the processes shown in Fig. 10 are presented in supplementary videos 3(a-c).

The bag formation occurs due to deformation of the whole front of a fast ripple. This process was first observed by Woodmansee and Hanratty (1969) who described the entrainment process as lifting, acceleration and subsequent scattering of ripples on top of disturbance waves. Alekseenko et al. (2009) noticed that the fast ripples disappear near the fronts of disturbance waves. They supposed that the fast ripples disappear because of being disrupted by the gas shear into droplets. This description is generally correct with two elaborations. First, entrainment events are not only initiated at the final stage of evolution of a fast ripple (namely, at the very front of disturbance wave, where fast ripples disappear). Liquid bags are often formed from the fast ripples from the third or fourth ‘layer’ from the front of disturbance wave. Simultaneously with the bag evolution, the ‘parent’ ripple is also accelerated and protruded forward to the front of disturbance wave, where it finally decays after the bag is disrupted. Example of video for such process is shown in supplementary video 4. Second, not all the ripples end by being scattered into droplets. Part of fast ripples propagates relatively slow towards the front of disturbance wave and decay in front of it without producing droplets. The higher the gas and liquid flow rates, the higher the probability that a particular ripple wave is disrupted. At the lowest gas and liquid flow rates (V_g=16 m/s and Re_L=155, 220) no droplets were observed at all, despite the presence of disturbance waves, covered by fast ripples. Example of passage of a single disturbance wave at low gas velocity is shown in supplementary video 5.

Quite often bag break-up is initiated by impact of a droplet onto the back slope of a fast ripple. In this case, a cavern surrounded with a high-amplitude rim appears due to droplet impact. The cavern expands, pushing the rim in front of it. The rim interacts with the crest of the fast ripple, making it unstable to the action of gas shear, and the bag is formed easily in this case. Example of such a process is presented in supplementary video 6.

In the case of ligament break-up, a tiny liquid jet appears in front of disturbance wave (see Fig. 11). It protrudes forward along its own axis and finally breaks into droplets. Length of the ligament may reach about 10 mm before it is broken and has a typical thickness of about 1 mm. Droplets, created by ligament break-up, are larger and slower than that created by bag break-up.

In contrast to the bag break-up, ligaments are formed at the junctions between two neighboring fast ripples. At such a junction longitudinally oriented stripe of larger film thickness appears, formed by the edges of two adjacent fast ripples, supported by the front of following fast ripple from behind. This structure serves as a source of ligament formation. Full videos of the processes shown in Fig. 11 are presented in supplementary videos 7(a-c).

It is interesting that both mechanisms occur at the same flow conditions and, moreover, on the same disturbance waves. It is not entirely consistent with the work of Azzopardi (1983), who marked the transition from bag to ligament break-up based on local minimum in dependence of droplet diameter on liquid superficial velocity. Fig. 12 shows this transition line and data of present work. The axes are scaled in terms of superficial gas velocity and liquid film Reynolds number. For the pipes film Reynolds number is defined as $q/\pi d\nu$, where q is volumetric liquid flow rate, d is pipe diameter and ν is kinematic viscosity of liquid. For the rectangular duct Re_L is defined as $q/W\nu$, where W is the width of the duct. It can be seen that the whole range of present data lie in the 'bag' region, except for the only point with the largest values of gas and liquid flow rates.

Ligament break-up events were observed in present experiments in the 'bag break-up region' very far from the transition line. Several ligaments were observed in the point Re_L=220, V_g=25 m/s. The entrainment events are very rare to observe farther from the transition line, and for V_g=16 m/s no droplets were observed at all.

So, the transition line should not be interpreted as a 'switch' between bag and ligament break-up mechanisms but something more gradual. We suppose that both bag and ligament break-ups occur in the whole range of entrainment conditions. But in the 'bag' region the probability of bag break-up occurrence is larger than that of ligament break-up, and vice

versa. Possibly, the transition line corresponds to conditions with equal contribution of the two mechanisms into total number or total volume of created droplets.

This idea fits the observations of Lecoeur et al. (2010) and Pham et al. (2014), who also observed both bag and ligament break-ups simultaneously. Lecoeur et al. report the occurrence of both mechanisms for V_g=11.6 m/s and superficial liquid velocity V_{sl} =0.036 m/s for stratified flow in 79 mm horizontal pipe. To recalculate V_{sl} into Re_L, width occupied by the liquid can be estimated as 54 mm, judging by the images presented in the paper. This gives Re_L=3260. Pham et al. counted nearly the same number of bag and ligament break-up events for V_g=60 m/s and Re_L=100.

The probability of ligament break-up is then expected to grow with gas and liquid flow rates, and the probability of bag break-up is expected to decrease with both quantities. This is consistent with the observations made in present paper. As we noted already, bag break-up occurs due to disruption of the whole front of a fast ripple, whereas ligament break-up occurs at the junctions between the fast ripples. The transverse size of fast ripples decreases with gas velocity (see Fig. 9b). Thus, at larger gas velocity, there will be larger number of junctions, which are potential sources of entrainment through ligament break-up. At the same time, narrower ripples are supposedly harder to break in 'bag' manner. So, the decrease in fast ripples' width explains the transition from bag to ligament break-up with increasing gas velocity at constant liquid flow rate.

Judging from the shape of the transition line, similar behavior of probabilities of bag and ligament break-ups should take place with increasing liquid flow rate at constant gas velocity. Nonetheless, the trend of decreasing the width of fast ripples with liquid flow rate is very weak. Thus, some additional considerations are required to explain this behavior. Possibly, this is related to larger height of longitudinally-oriented liquid structures in the junctions between fast ripples at larger liquid flow rates.

5. Conclusions

High-speed laser-induced fluorescence technique has been applied to study the gas-sheared liquid film in a horizontal rectangular duct with dimensions 161 mm by 25 mm. The evolution of waves of different types has been studied longitudinally, transversely, and over an area with time. The mechanisms of entrainment of liquid from film surface were also studied.

Disturbance waves generate ripples on their back slopes. New ripples can move either faster or slower than parent disturbance waves. The ‘slow ripples’ slide to the base film behind the disturbance wave and travel with low speed until the following disturbance wave absorbs them. The ‘fast ripples’ move over the disturbance wave’s top and disappear near the fronts of disturbance waves. They also are the source of liquid entrainment. This process is qualitatively the same as that described by Alekseenko et al. (2009) for downward flow in narrow vertical pipe. Thus, generation of fast and slow ripples by disturbance waves is expected to happen in any annular flow with entrainment, for any shape, size and orientation of the duct, independently on the properties of disturbance waves.

The disturbance waves are localized by the transverse coordinate and have curved fronts. The initial disturbance waves, which are produced not far from the inlet, supposedly have small width and high curvature. Further downstream edges of neighboring narrow waves coalesce to form wider and less curved waves. Thus, the disturbance waves become more two-dimensional downstream.

Both fast and slow ripples are localized by the transverse coordinate and have curved fronts. The fast ripples are placed on tops of disturbance waves in staggered order in several transverse ‘layers’. Velocity, width and curvature of fast ripples may vary greatly on the same disturbance wave. At larger gas velocities the fast ripples are narrower and more curved. The average velocity of fast ripples is about 20-30% larger than the average velocity of disturbance waves.

Three mechanisms of liquid entrainment were observed: bag and ligament break-up of the fast ripples and secondary entrainment due to droplet impacts on film surface. Bag and ligament break-up coexist in a wide range of flow parameters far from the bag-to-ligament transition line defined by Azzopardi (1983). Supposedly, the transition line corresponds to the region where contribution of the two mechanisms to total entrainment is the same.

Bag and ligament break-up can occur at any fast ripple, irrespectively on the distance to the front of disturbance wave. Part of fast ripples decay in front of disturbance wave without contributing to entrainment. Probability of entrainment event increases with gas and liquid flow rates. It is also observed that the bag break-up can be initiated by a droplet, impacting at the rear slope of a fast ripple.

An explanation of difference between the two break-up mechanisms is proposed. The bag break-up occurs when the whole front of a fast ripple is torn; the ligament break-up occurs at the junction of the edges of two neighboring fast ripples. With the increase in gas velocity, the number of junctions between the fast ripples increases, and the fronts of fast ripples

become narrower, and, possibly harder to break. This explains the increase in relative probability of ligament break-up with gas velocity.

Acknowledgements: The work was supported by UK EPSRC Program Grant MEMPHIS (EP/K003976/1). Authors are grateful to the Roll-Royce UTC (University of Nottingham) for access to the flow facility. Andrey Cherdantsev is grateful for support to Russian Foundation for Basic Research (project 13-08-1400a) and to President of Russian Federation (project MK-5997.2014.1).

References:

Adomeit, P., Renz, U., 2000. Hydrodynamics of three-dimensional waves in laminar falling films. Int. J. Multiphase Flow, 26:1183-1208

Alamu, M.B., Azzopardi, B.J. (2011) Wave and drop periodicity in transient annular flow. Nucl Eng Des 241:5079-5092

Alekseenko, S.V., Antipin, V.A., Cherdantsev, A.V., Kharlamov, S.M., Markovich, D.M., (2009) Two-wave structure of liquid film and waves interrelation in annular gas-liquid flow with and without entrainment, Phys Fluids 21: 061701-061704.

Alekseenko, S., Cherdantsev, A., Cherdantsev, M., Isaenkov, S., Kharlamov, S., Markovich, D. (2012) Application of a high-speed laser-induced fluorescence technique for studying the three-dimensional structure of annular gas–liquid flow. Exp Fluids 53:77–89

Alekseenko, S.V., Cherdantsev, A.V., Markovich, D.M., Rabusov, A.V. (2014a) Investigation of droplets entrainment and deposition in annular flow using LIF technique. Atomization and Sprays, 24 (3): 193–222.

Alekseenko, S.V., Cherdantsev A.V., Cherdantsev M.V., Isaenkov S.V., Markovich D.M. (2014b) LIF investigation of disturbance waves' properties in downward annular flow in 11.7 mm pipe (in preparation).

Alghoul, S. (2011) Experimental investigation of a single droplet impact on the moving films. Ph.D. Thesis, University Of Nottingham, Nottingham, UK.

Azzopardi, B.J. (1983) Mechanisms of entrainment in annular two-phase flow. *UKAEA Report AERE-R* 11068.

Azzopardi, B.J. (1986) Disturbance wave frequencies, velocities and spacing in vertical annular two-phase flow. Nucl Engng Des 92:121–133

Azzopardi, B.J. (1997) Drops in annular two-phase flow. Int J Multiphase Flow 23, Suppl.: 1-53

Belt, R.J., Van't Westende, J.M.C., Prasser, H.-M., Portela, L.M. (2010) Time and spatially resolved measurements of interfacial waves in vertical annular flow. Int J Multiphase Flow 36:570–587

Chu, K.J., Dukler, A.E. (1974) Statistical characteristics of thin, wavy films: Part II. Studies of the substrate and its wave structure. AIChE J 20:695–706

Chu, K.J., Dukler, A.E. (1975) Statistical characteristics of thin, wavy films III. Structure of the large waves and their resistance to gas flow. AIChE J 21:583–593

Clark, W.W., Campbell, G.B., Hills, J.H., Azzopardi, B.J., 2001. Viscous effects on the interfacial structure of falling liquid film / co-current gas systems. 4th Int. Conf. Multiphase Flow, 27 May - 1 June 2001, New Orleans, USA.

Demekhin, E.A., Kalaidin, E.N., Kalliadasis, S., Vlaskin, S. Yu., 2007. Three-dimensional localized coherent structures of surface turbulence. I. Scenarios of two-dimensional–three-dimensional transition. Phys Fluids 19: 114103

Hall Taylor, N.S., Hewitt, G.F., Lacey, P.M.C. (1963) The motion and frequency of large disturbance waves in annular two-phase flow of airwater mixtures. Chem Eng Sci 18:537–552

Hall Taylor, N.S., Nedderman, R.M. (1968) The coalescence of disturbance waves in annular two phase flow. Chem Engng Sci 23:551–564

Han, H., Zhu, Z., Gabriel, K. (2006) A study on the effect of gas flow rate on the wave characteristics in two-phase gas–liquid annular flow. Nucl Engng Des 236:2580–2588

Lecoeur, N., Hale, C.P., Spelt, P.D.M., Hewitt, G.F., (2010) Visualization of droplet entrainment in turbulent stratified pipe flow, Proc. of 7th Int. Conf. Multiphase Flow, paper 14.1.5.

Okada, O., Fujimatsu, T., Fujita, H. and Nakajima, Y. (1995) Measurement of droplet size distribution in an annular mist flow in a vertical pipe by immersion liquid method. Proc. 2nd. Int. Conf on Multiphase Flow, Kyoto, Vol. 1, pp. IP2/11-IP2/18.

Pham, S.H., Kawara, Z., Yokomine, T., Kunugi, T. (2014) Detailed observations of wavy interface behaviors of annular two-phase flow on rod bundle geometry. Int J Multiphase Flow, 59:135–144

Sawant, P., Ishii, M., Hazuku, T., Takamasa, T., Mori, M. (2008) Properties of disturbance waves in vertical annular two-phase flow. Nucl Engng Des 238:3528–3541

Schubring, D., Shedd, T.A., Hurlburt, E.T. (2010) Planar laser-induced fluorescence (PLIF) measurements of liquid film thickness in annular flow. Part II: Analysis and comparison to models. Int J Multiphase Flow, 36:825–835

Takamasa, T., Hazuku, T. (2000) Measuring interfacial waves on fim flowing down a vertical plate wall in the entry region using laser focus displacement meters. Int J Heat Mass Transfer 43 2807-2819

Wilkes, N.S., Azzopardi, B.J., Thompson, C.P., (1983) Wave coalescence and entrainment in vertical annular two-phase flow, Int. J. Multiphase Flow, 9:383-398.

Woodmansee, D.E., Hanratty, T.J., (1969) Mechanism for the removal of droplets from a liquid surface by a parallel air flow, *Chem. Engng. Sci.*, 24:299-307.

Zhao, Y., Markides, C.N., Matar, O.K., Hewitt, G.F., (2013) Disturbance wave development in two-phase gas–liquid upwards vertical annular flow, Int J Multiphase Flow, 55:111–129.

Figure captions:

Figure 1. Scheme of experimental setup. Flow loop (a); Inlet section (b); Cross-section of the duct (c).

Figure 2. Two fragments of matrix $h(t,x)$ for Re_L=360, V_g=35 m/s. 1 – slow ripples, 2 – fast ripples, 3 – liquid droplets, 4 – air bubbles.

Figure 3. Average velocity (a) and passing frequency (b) of disturbance waves. Present experiments: Re_L=155 (1); Re_L =220 (2); Re_L=360 (3); Re_L=520 (4). Data for downward flow in 11.7 mm i.d. pipe by Alekseenko et al. (2014b): Re_L=370 (5); Re_L=510 (6).

Figure 4. Example of instantaneous profile of film thickness obtained by LIF method for Re_L=360 and V_g=30 m/s. Flow direction is from left to right.

Figure 5. Fragments of *y-t* surface of film thickness. Parabolic approximations of individual disturbance waves are marked by solid black lines. Re_L=220. V_g=20 (a), 25 (b), 30 (c) and 35 (d) m/s. A longitudinal tail behind the edge of a disturbance wave (1); localized troughs behind the central part of a disturbance wave (2); longitudinal tails behind the central parts of disturbance waves (3).

Figure 6. Curvature *vs* width of individual disturbance waves. Re_L=220 (1-4); Re_L=360 (5-8). V_g=20 m/s (1,5); V_g =25 m/s (2,6); V_g =30 m/s (3,7); V_g =35 m/s (4,8).

Figure 7. Coalescence of edges of two disturbance waves. Re_L=220, V_g=35 m/s. Time delay between frames 1-2 and 2-3 is 16 ms and 22 ms, respectively.

Figure 8. Instantaneous shape of fast ripples on a disturbance wave. Re_L=360, V_g=20 m/s (a), 25 m/s (b), 30 m/s (c), 35 m/s (d). Size of each image is 50 mm * 50 mm. Junction of edges of two fast ripples is marked by (1).

Figure 9. Average velocity (a), width (b), curvature (c) and length (d) of fast ripples.

Figure 10. Examples of the bag break-up events. a) Re_L=220, V_g=30 m/s, area size 30*15

mm; b) Re_L=360, V_g =30 m/s, area size 20*13 mm; c) Re_L=520, V_g =35 m/s, area size 24*11 mm. Time grows downwards; time step is 0.5 ms for all the images.

Figure 11. Example of ligament break-up events. a) Re_L=220, V_g =30 m/s, area size 20*10 mm; b) Re_L=360, V_g =30 m/s, area size 30*14 mm; c) Re_L=520, V_g =35 m/s, area size 25*14 mm. Time grows downwards; time step is 0.5 ms for all the images.

Figure 12. Transition line from bag to ligament break-up mechanisms (1), proposed by Azzopardi (1983); the current range of experimental conditions (2); regimes with no droplets detected (3).

Supplementary materials:

Video 1. Coalescence of two disturbance waves. Re_L=220, V_g=35 m/s. Area size is 100 mm * 50 mm. Video is 400 times slower than the real process.

Video 2. Passage of a single disturbance wave across the area of measurements. Re_L=220, V_g=30 m/s. Area size is 100 mm * 50 mm. Video is 400 times slower than the real process.

Video 3. Examples of bag break-up events. a) Re_L=220, V_g=30 m/s, area size 25*14 mm; b) Re_L=360, V_g =30 m/s, area size 30*13 mm; c) Re_L=520, V_g =35 m/s, area size 30*15 mm. Videos are 2000 times slower than the real process.

Video 4. Example of bag break-up from a fast ripple far from the front of disturbance wave. Re_L=360, V_g =30 m/s, area size 35*15.6 mm. Video is 2000 times slower than the real process.

Video 5. Passage of a single disturbance wave across the area of measurements. Re_L=220, V_g=16 m/s. Area size is 100 mm * 50 mm. Video is 400 times slower than the real process.

Video 6. Example of bag break-up initiated by a droplet impact on a fast ripple. Re_L=220, V_g=30 m/s. Area size is 50 mm * 25 mm. Video is 2000 times slower than the real process.

Video 7. Examples of ligament break-up events. a) Re_L=220, V_g=30 m/s, area size 25*10 mm; b) Re_L=360, V_g =30 m/s, area size 38.5*15.5 mm; c) Re_L=520, V_g =35 m/s, area size 30*16 mm. Videos are 2000 times slower than the real process.

Xvid codec (https://www.xvid.com/download/) is required to watch the video files.

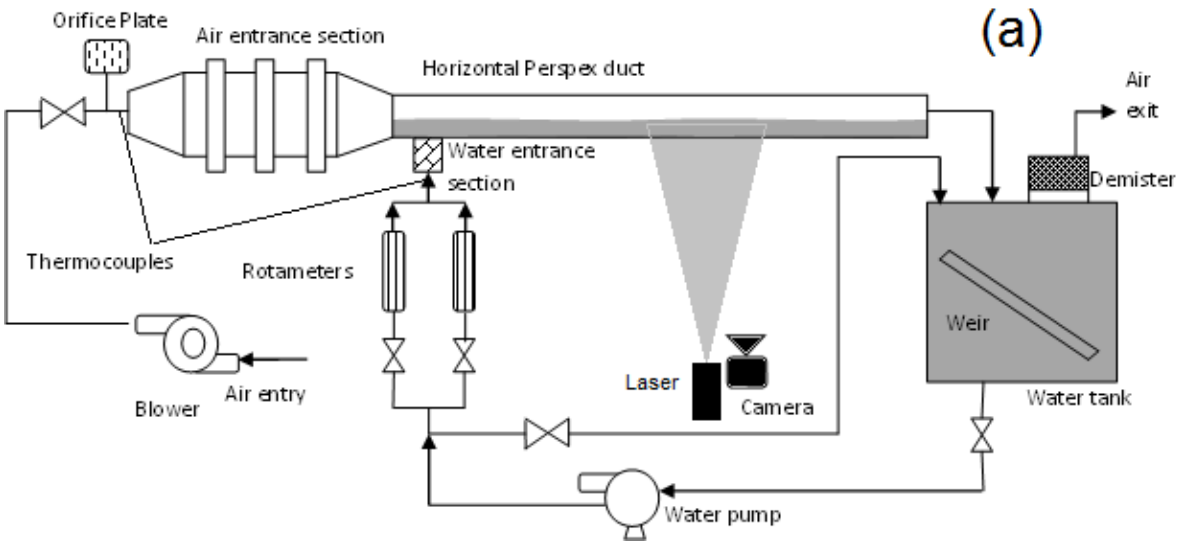

Diagram 1a

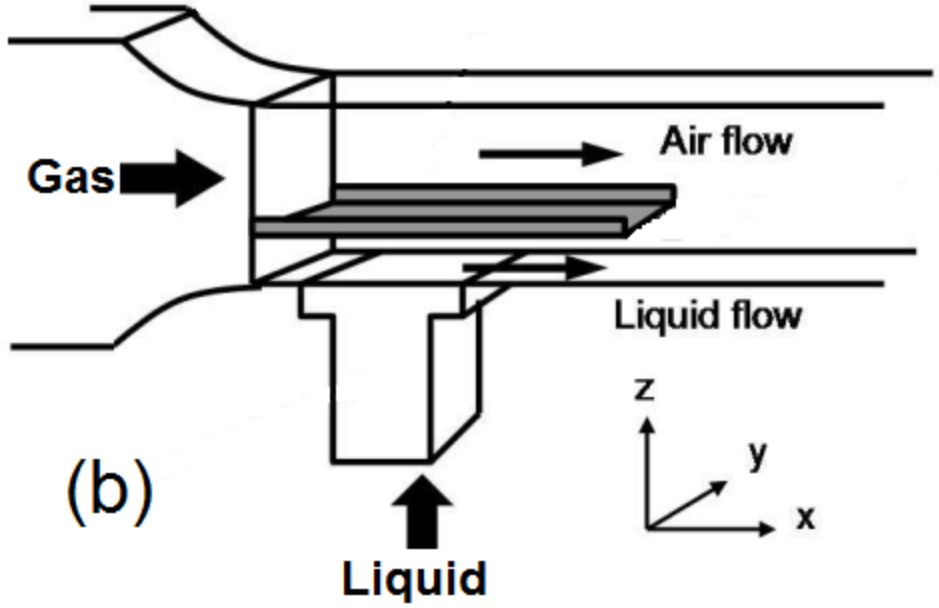

Diagram 1b

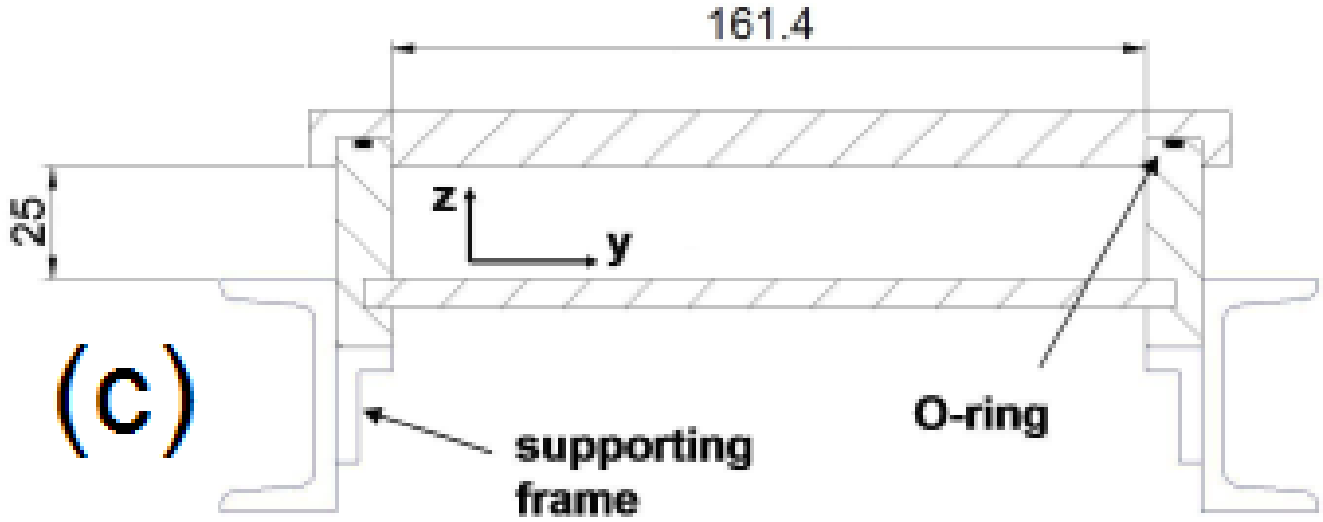

Diagram 1c

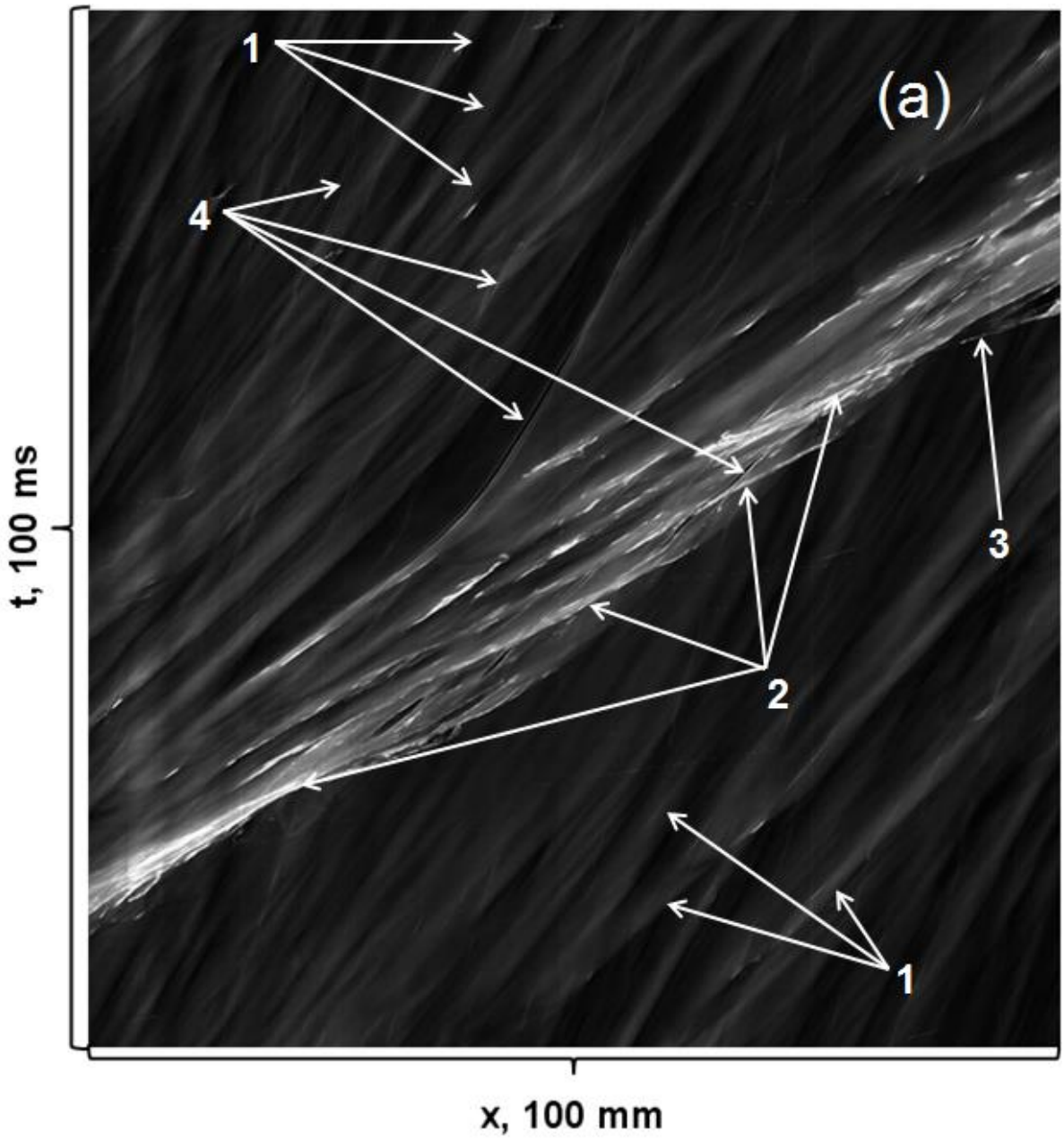

Diagram 2a

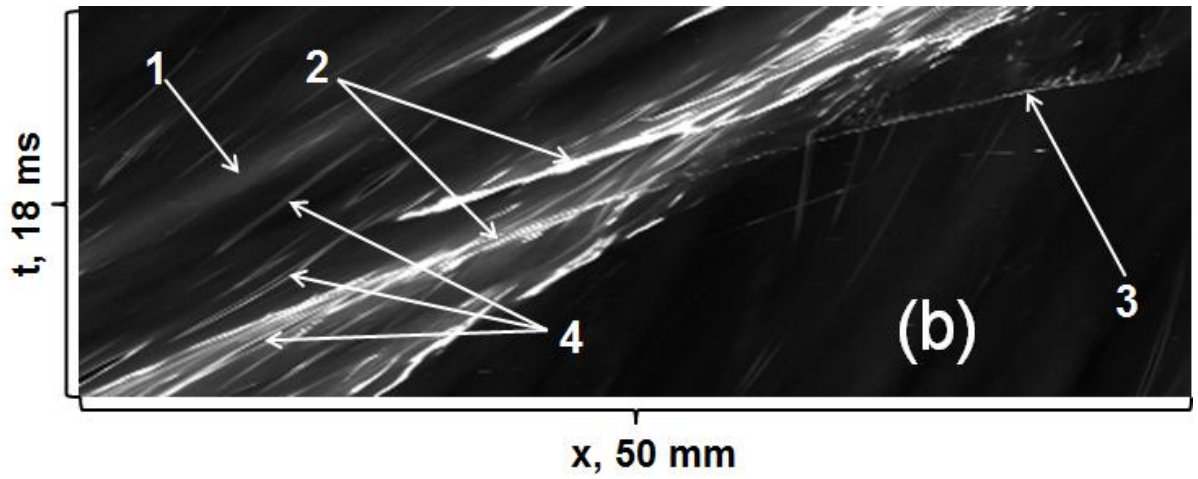

Diagram 2b

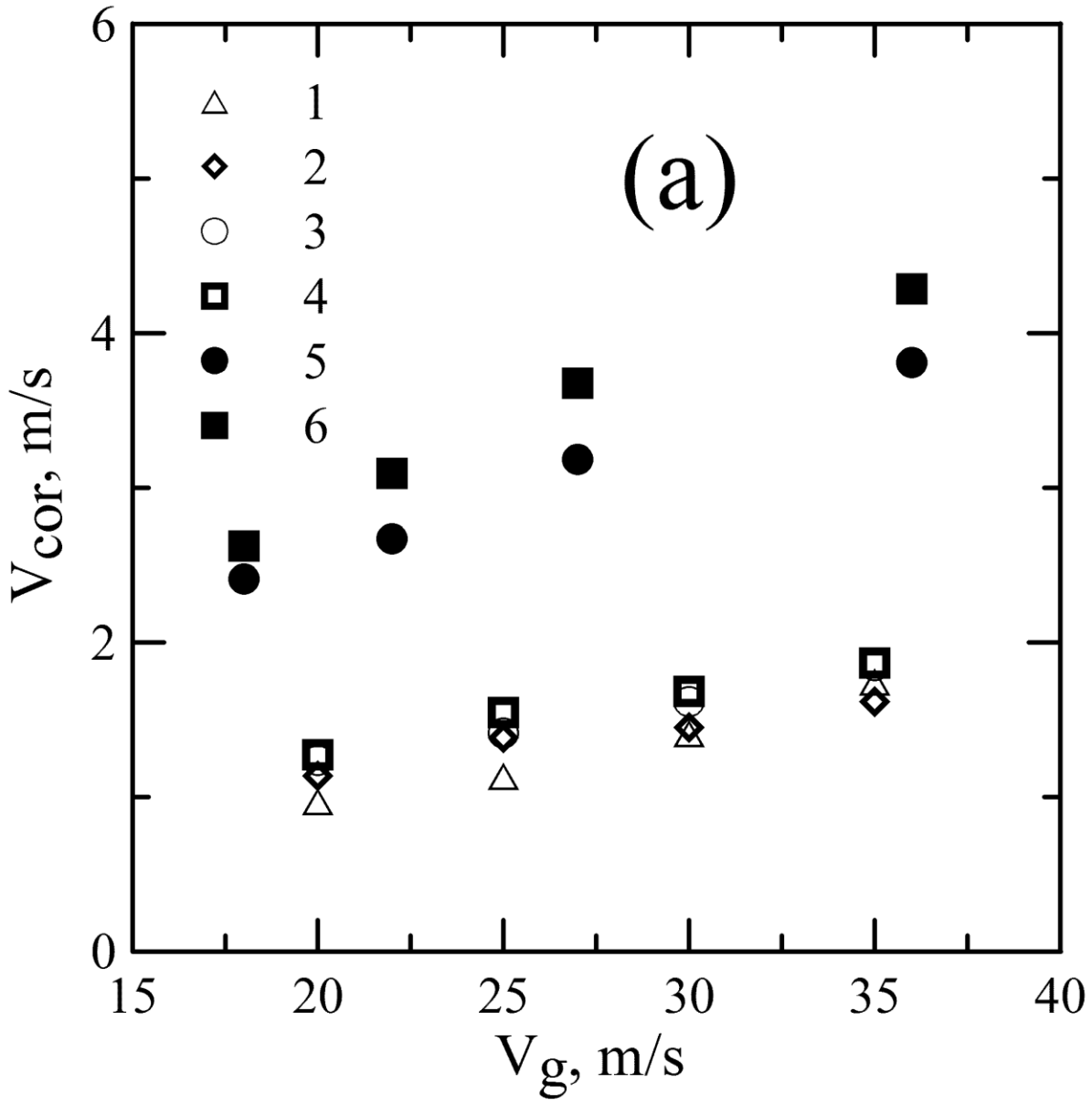

Diagram 3a

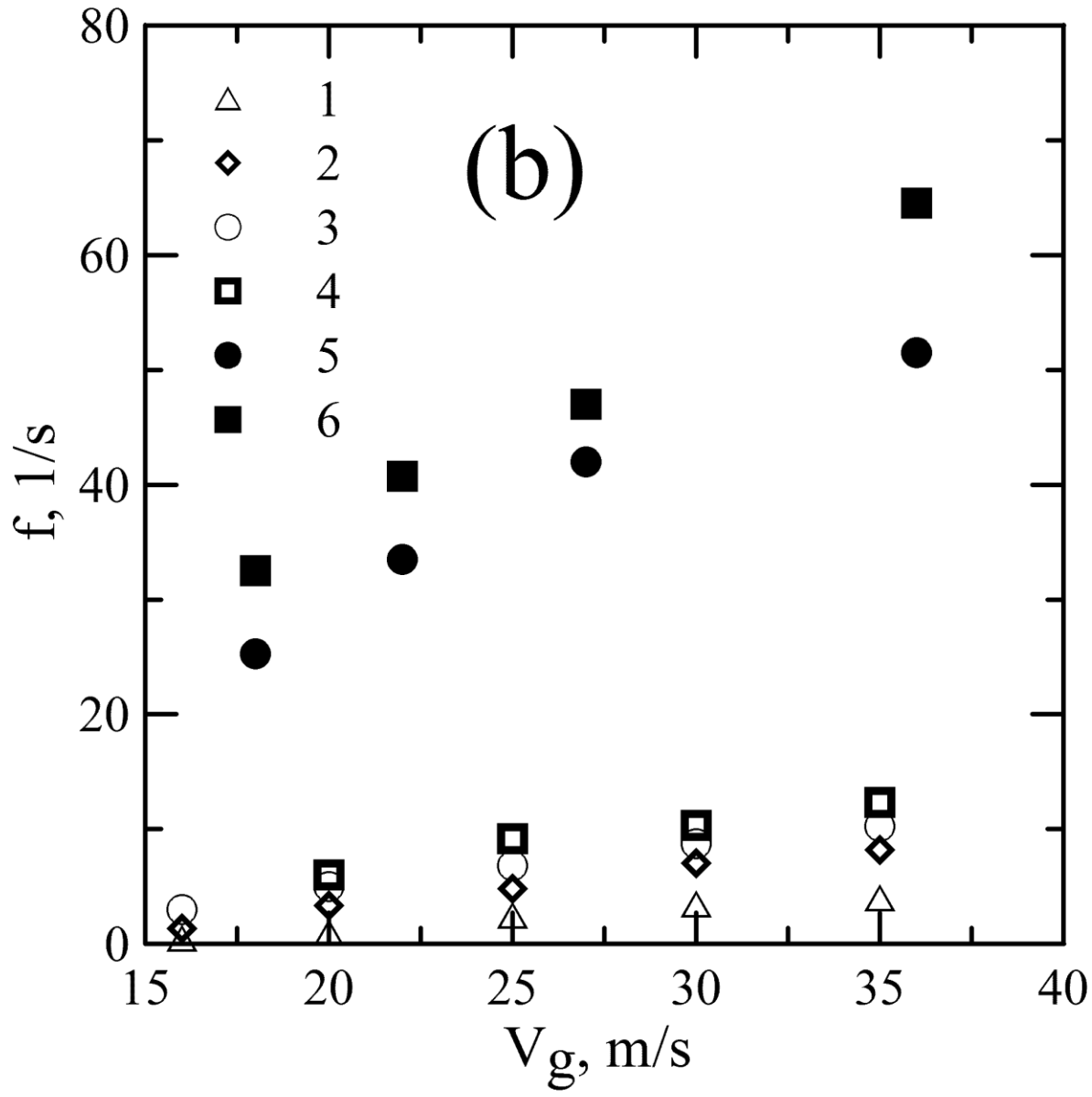

Diagram 3b

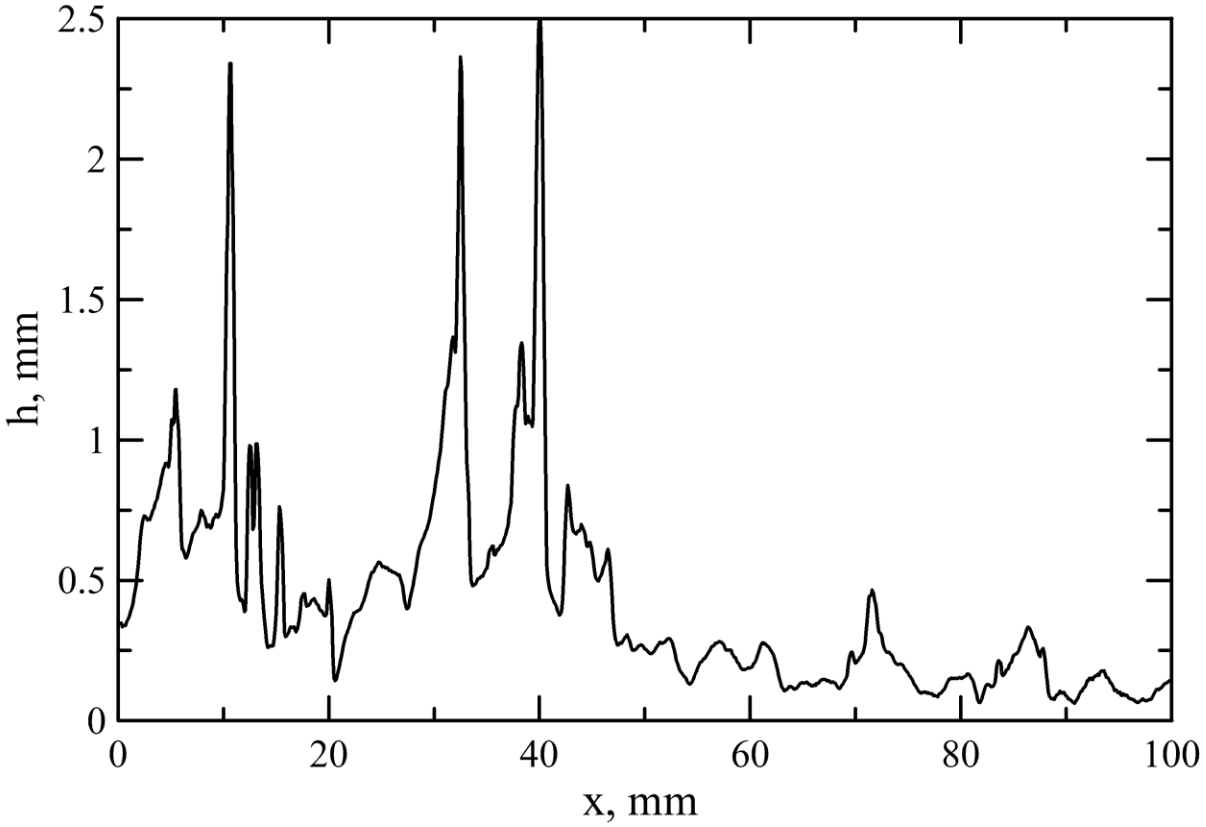

Diagram 4

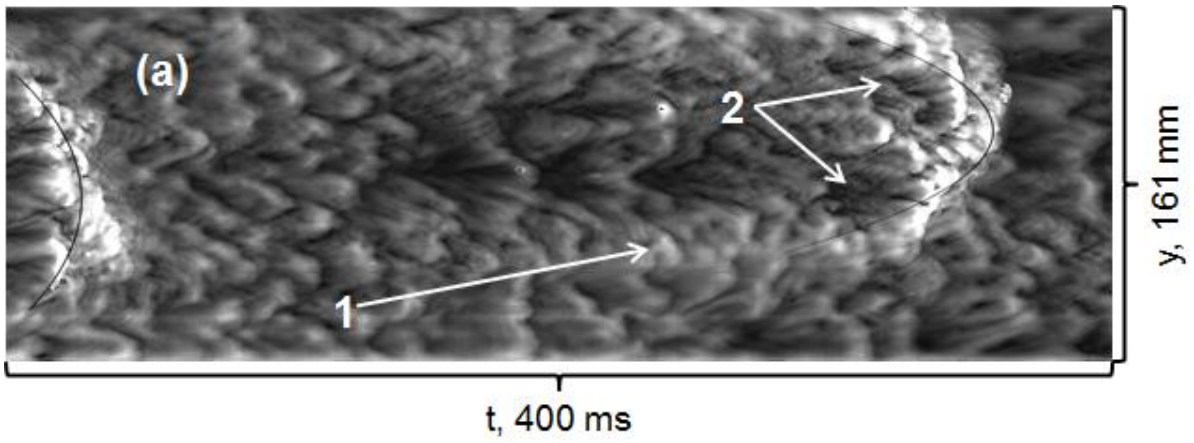

Diagram 5a

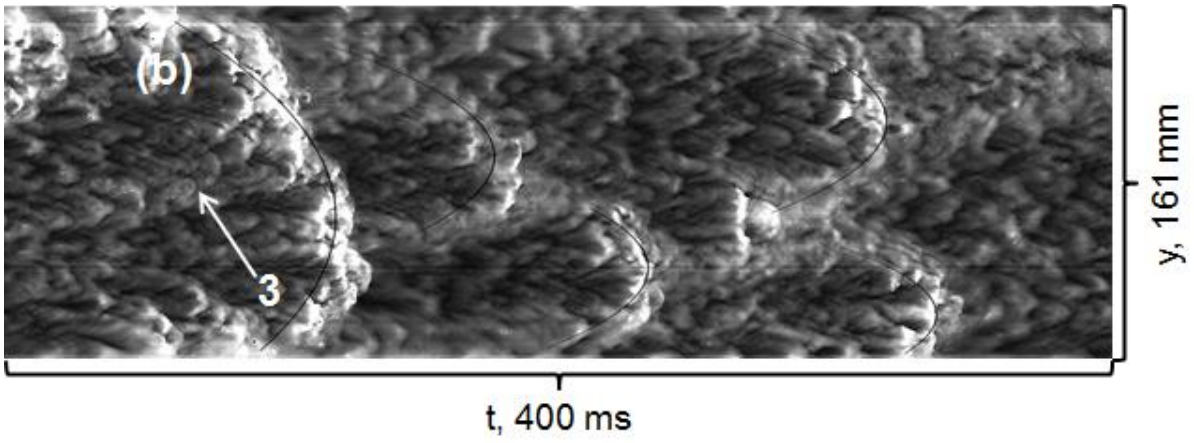

Diagram 5b

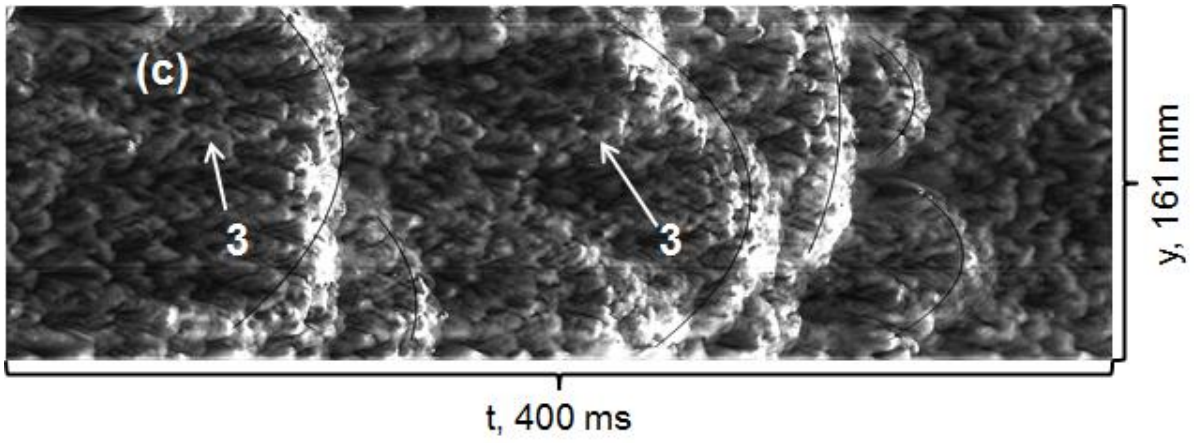

Diagram 5c

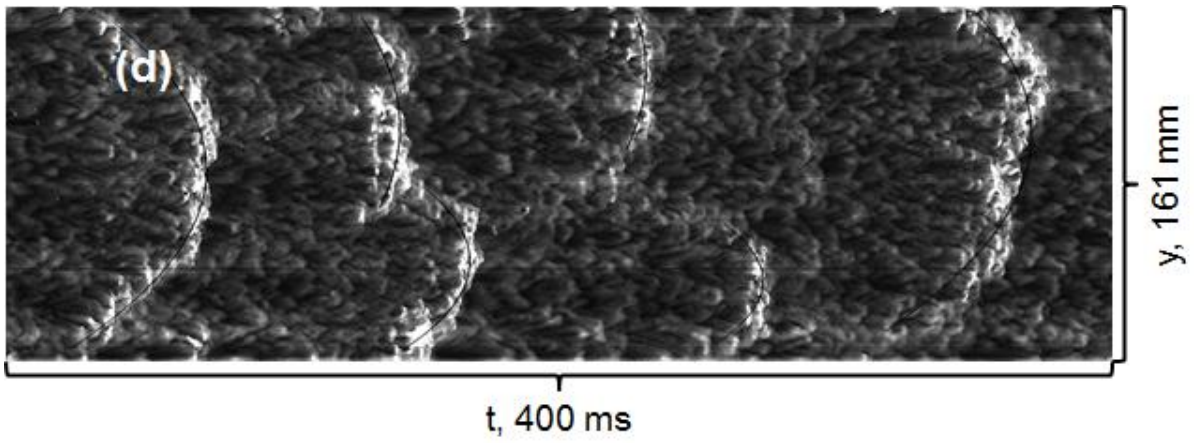

Diagram 5d

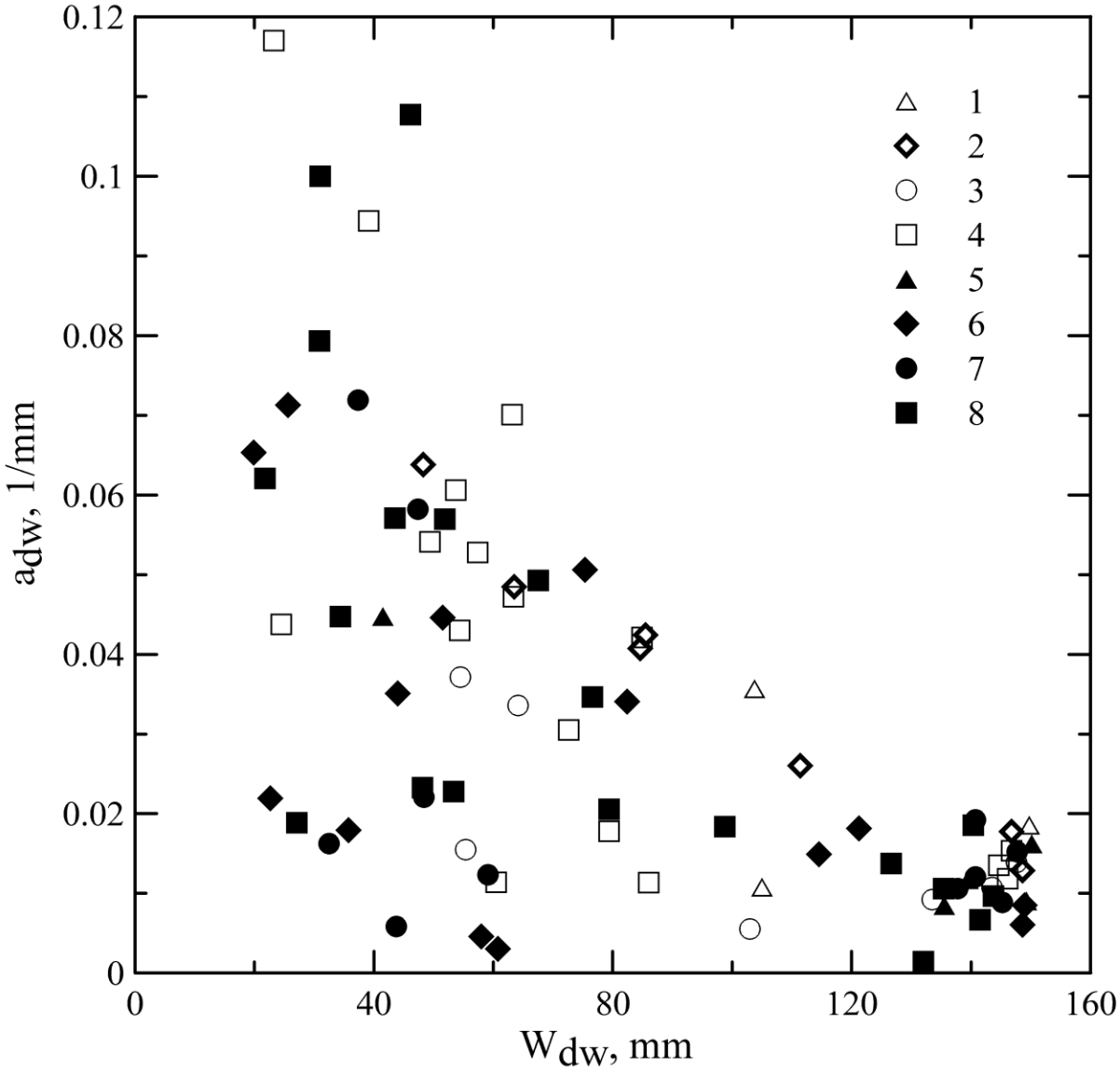

Diagram 6

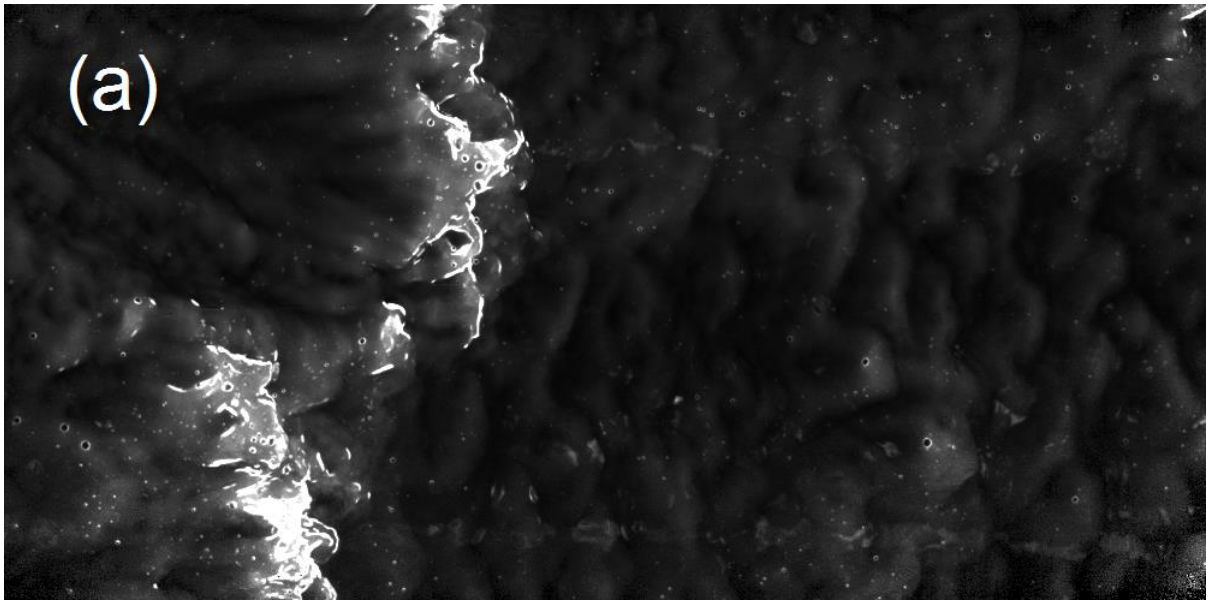

Diagram 7a

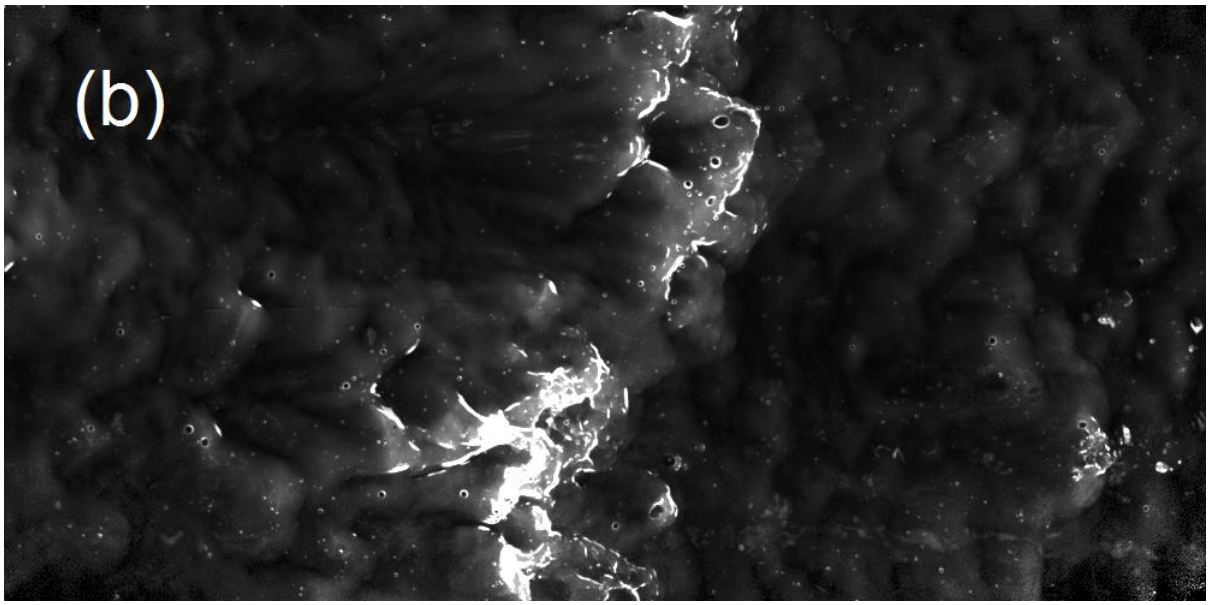

Diagram 7b

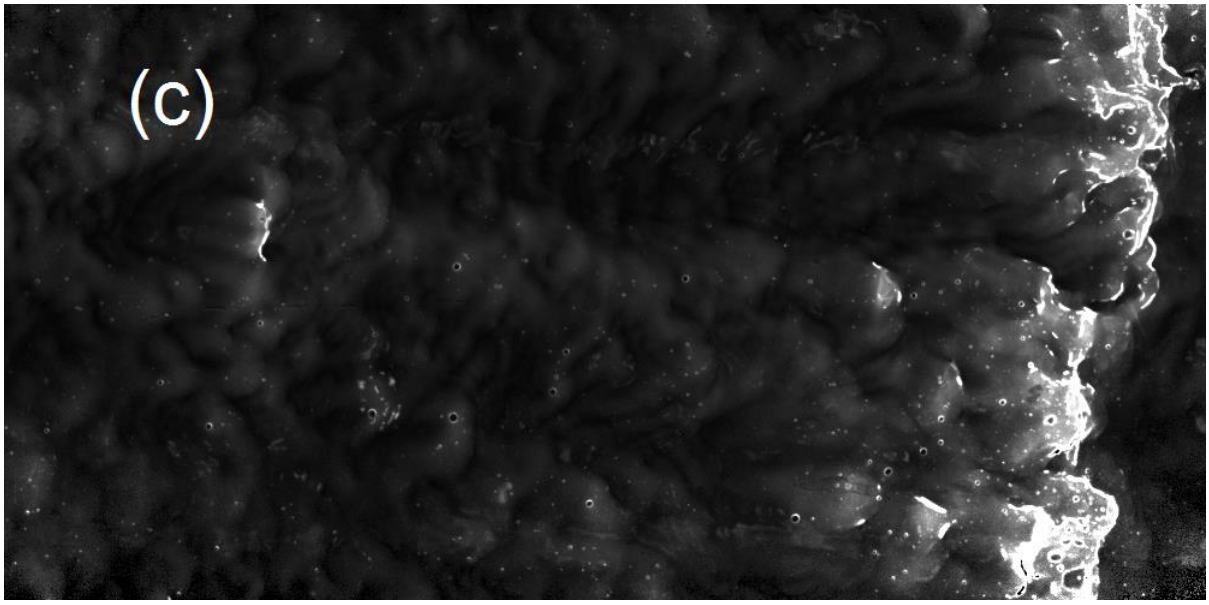

Diagram 7c

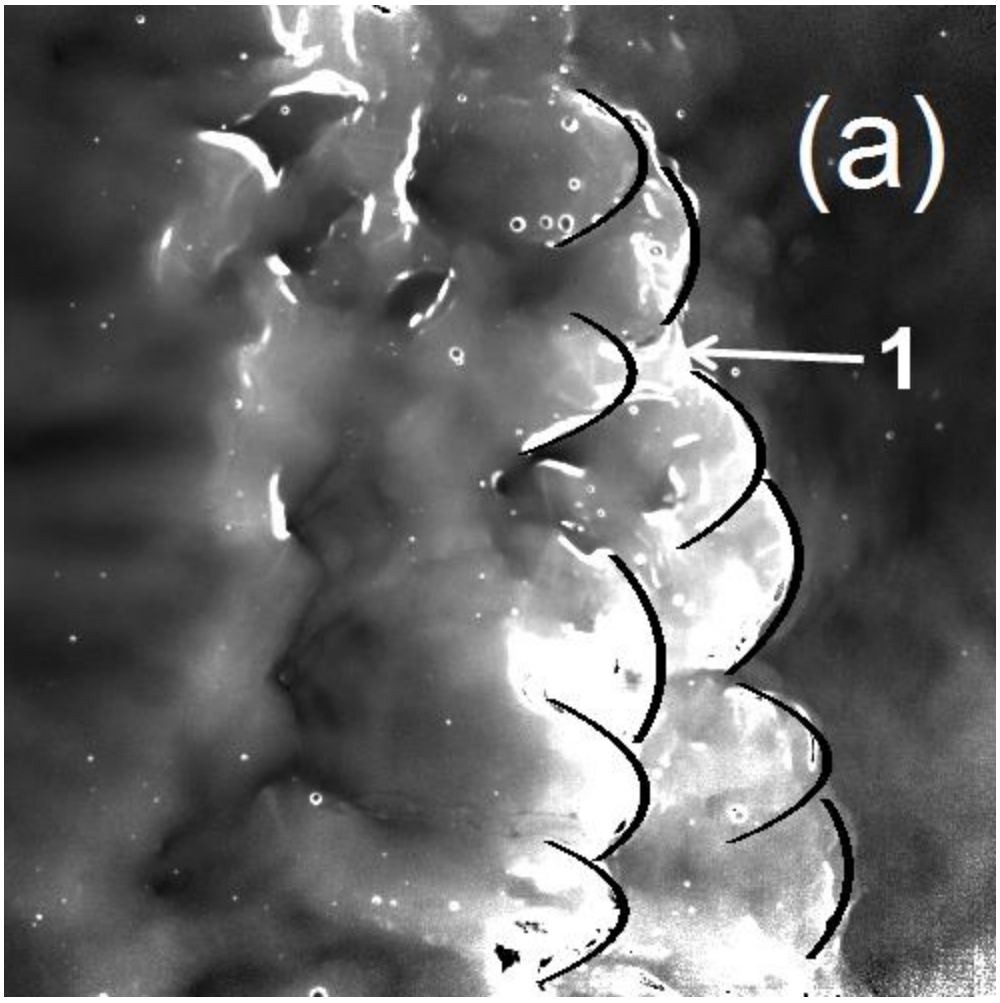

Diagram 8a

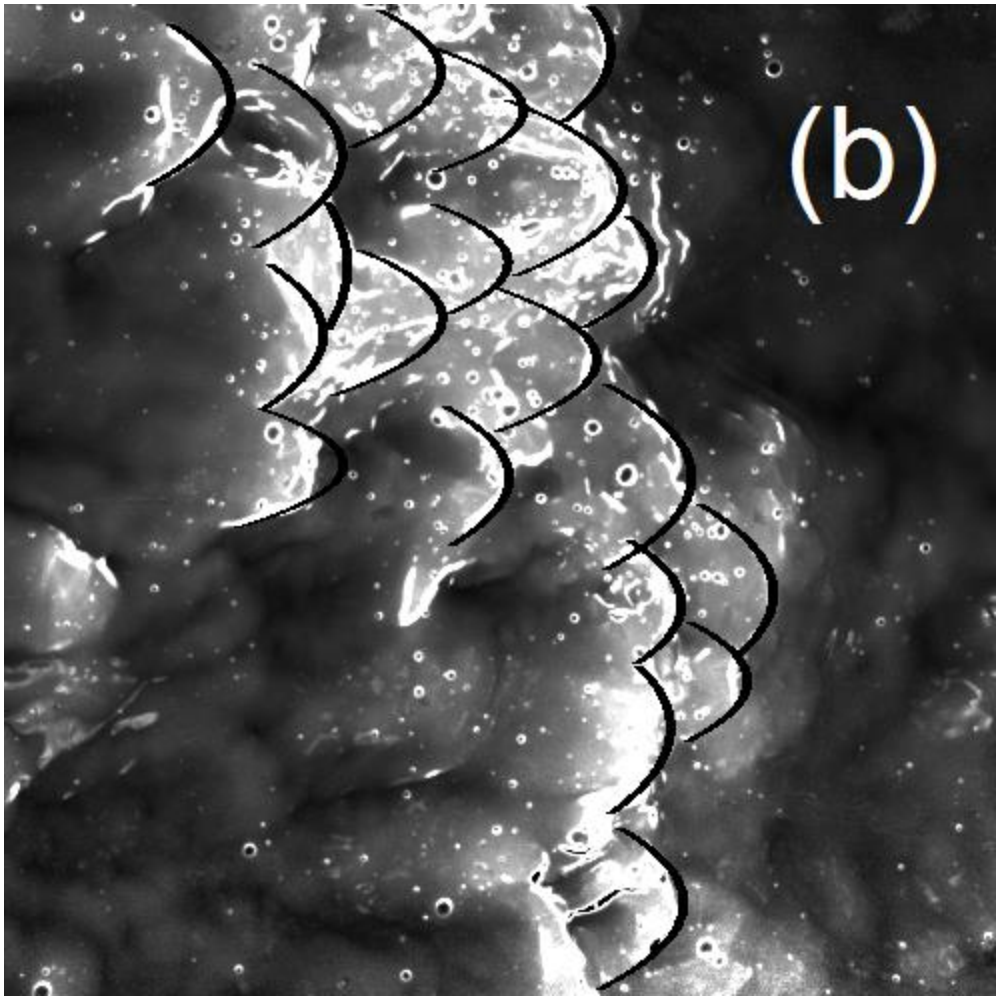

Diagram 8b

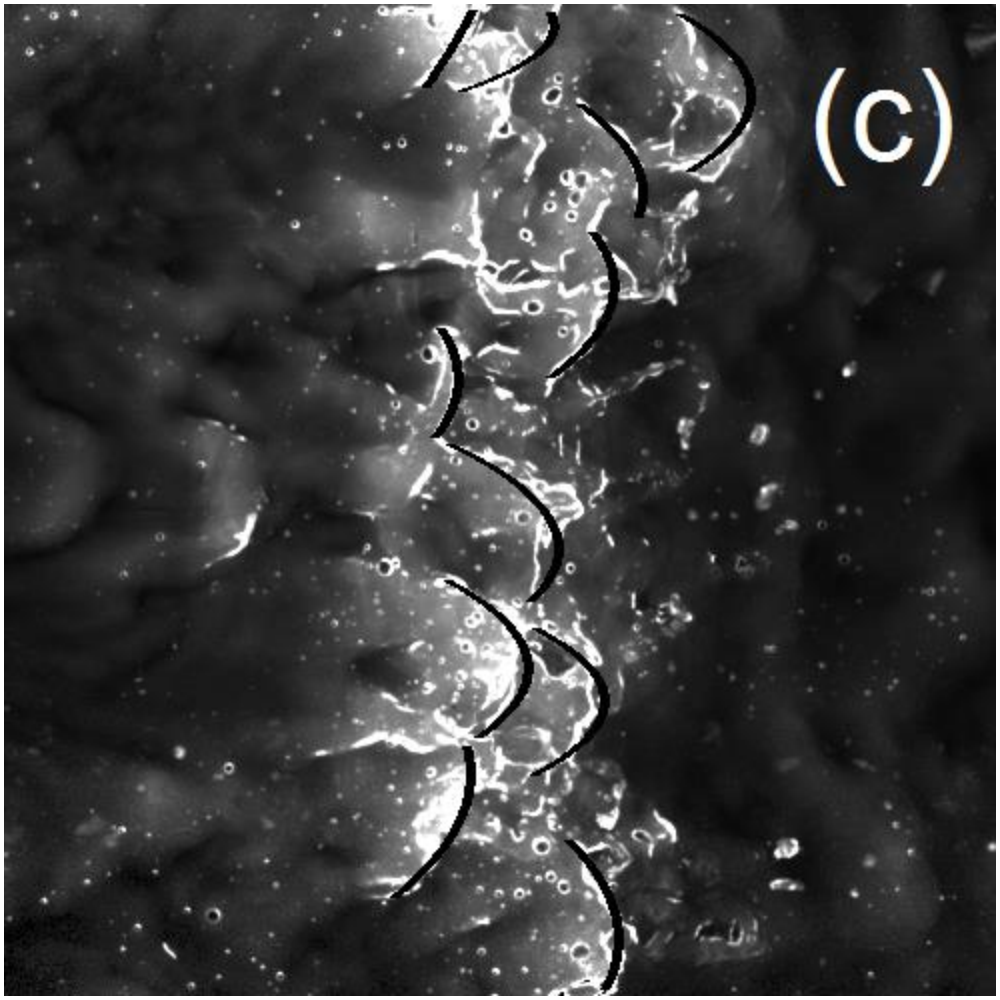

Diagram 8c

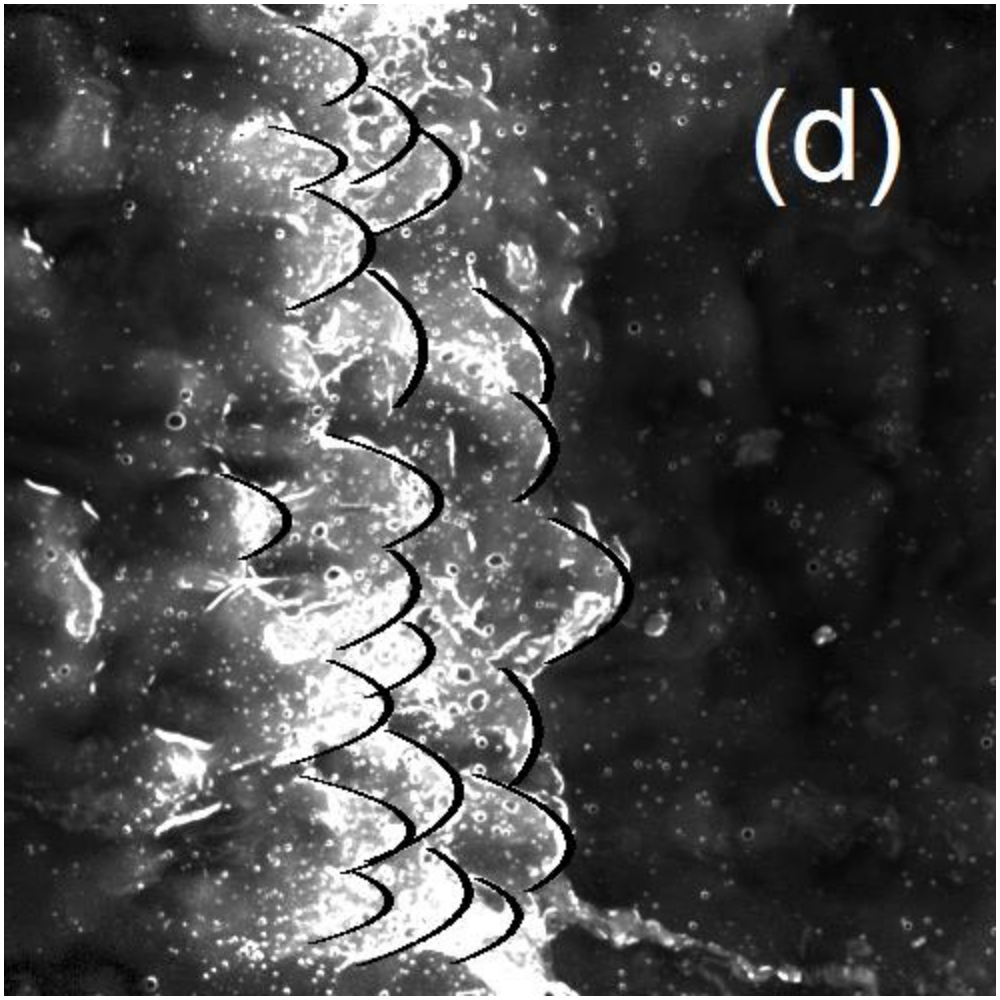

Diagram 8d

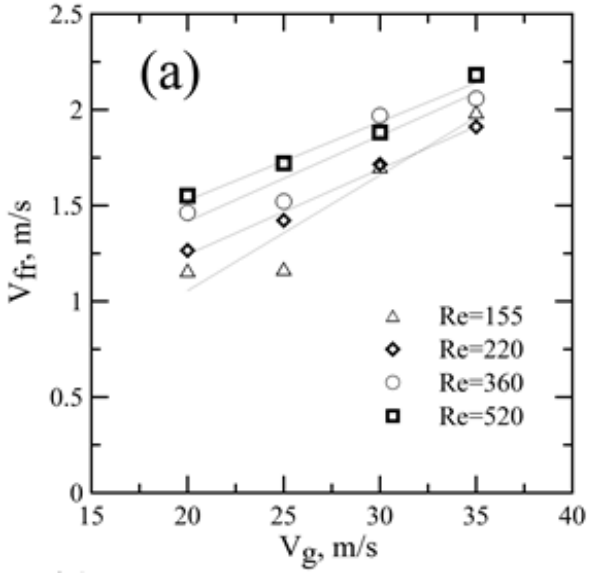

Diagram 9a

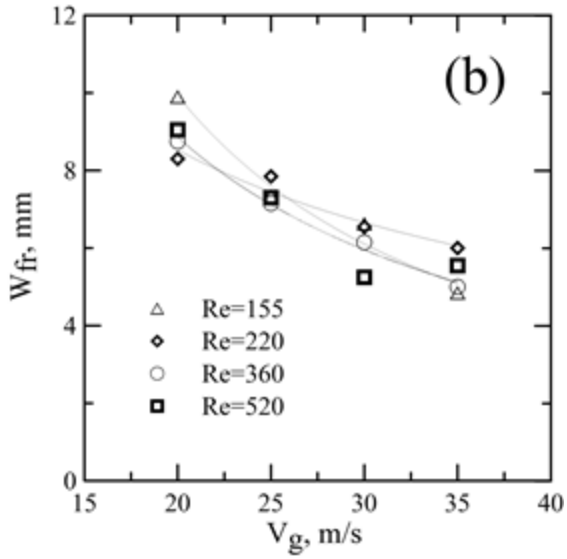

Diagram 9b

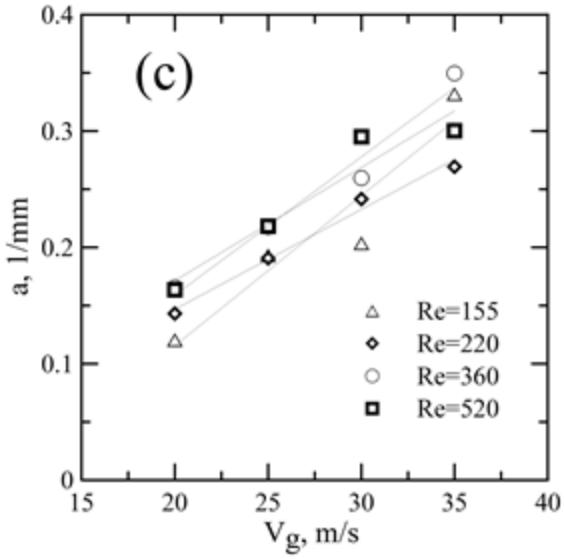

Diagram 9c

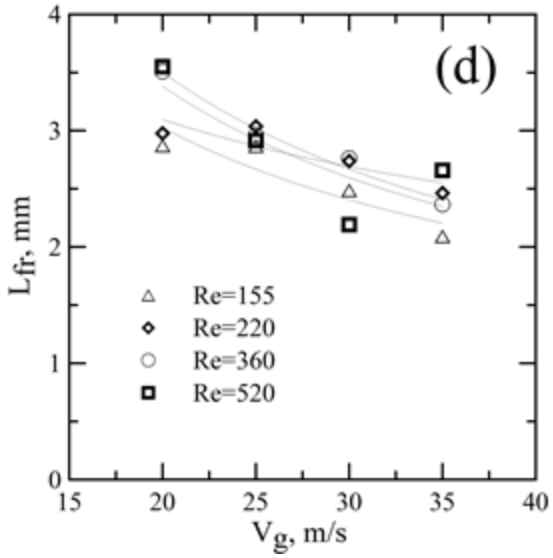

Diagram 9d

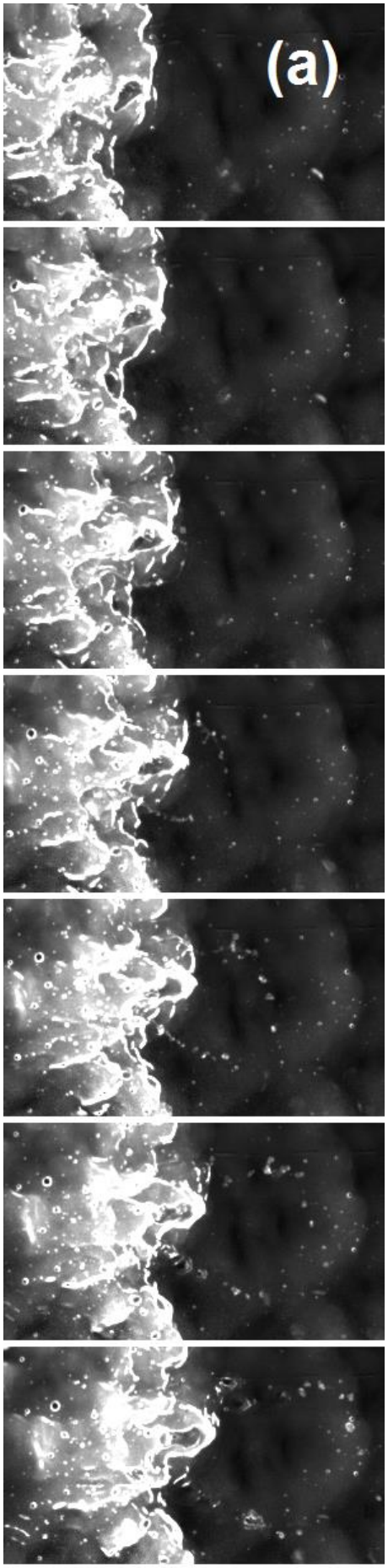

Diagram 10a

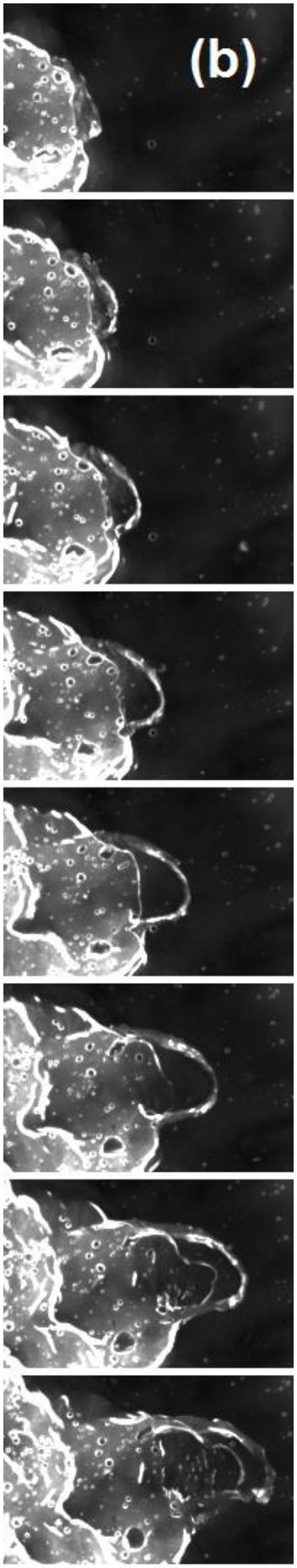

Diagram 10b

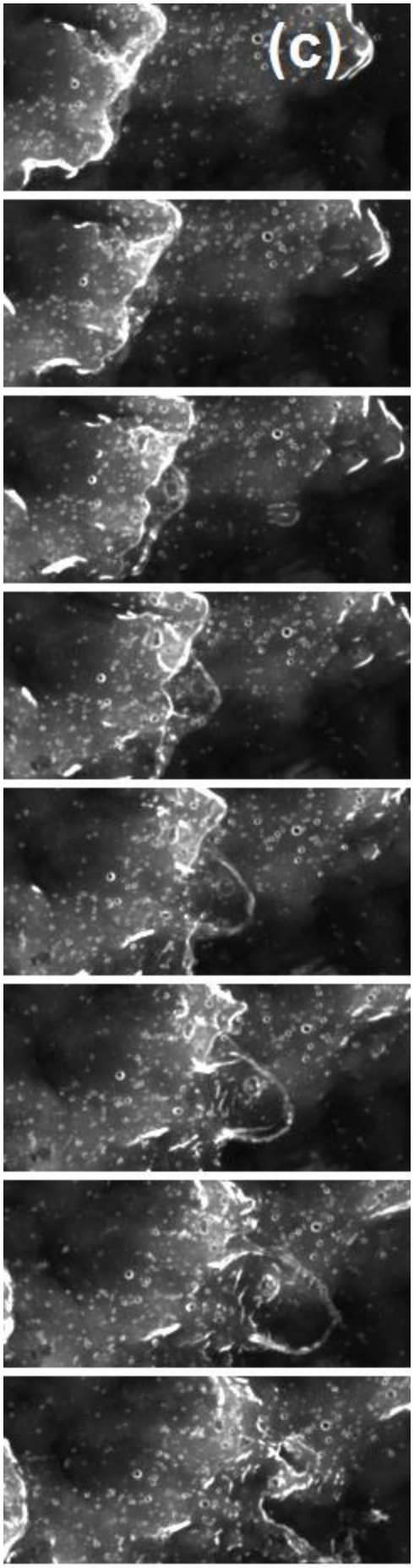

Diagram 10c

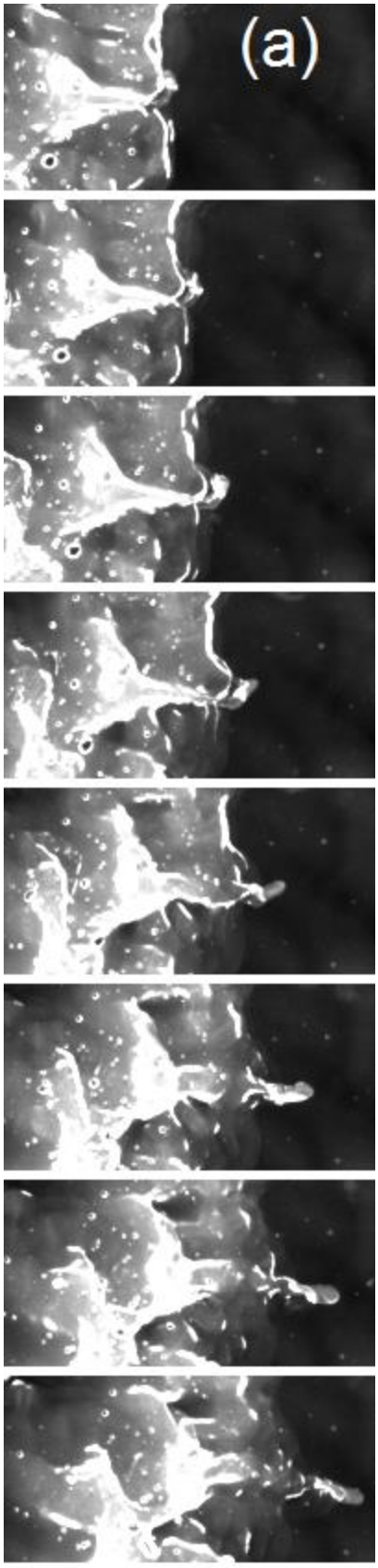

Diagram 11a

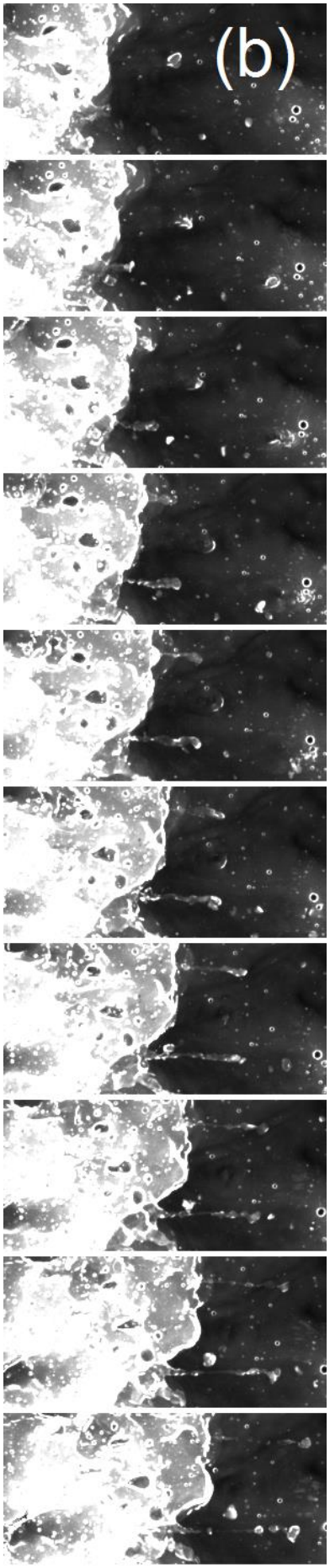

Diagram 11b

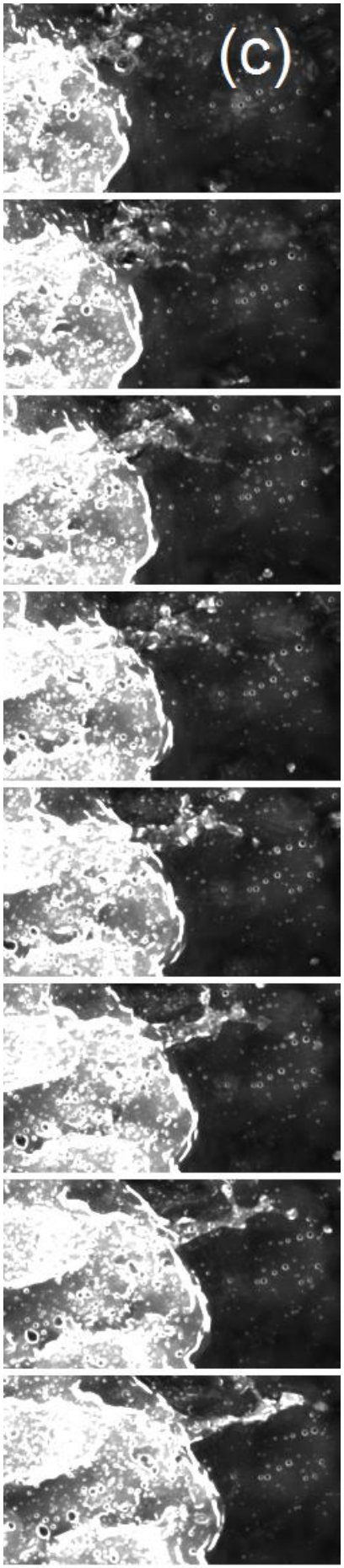

Diagram 11c

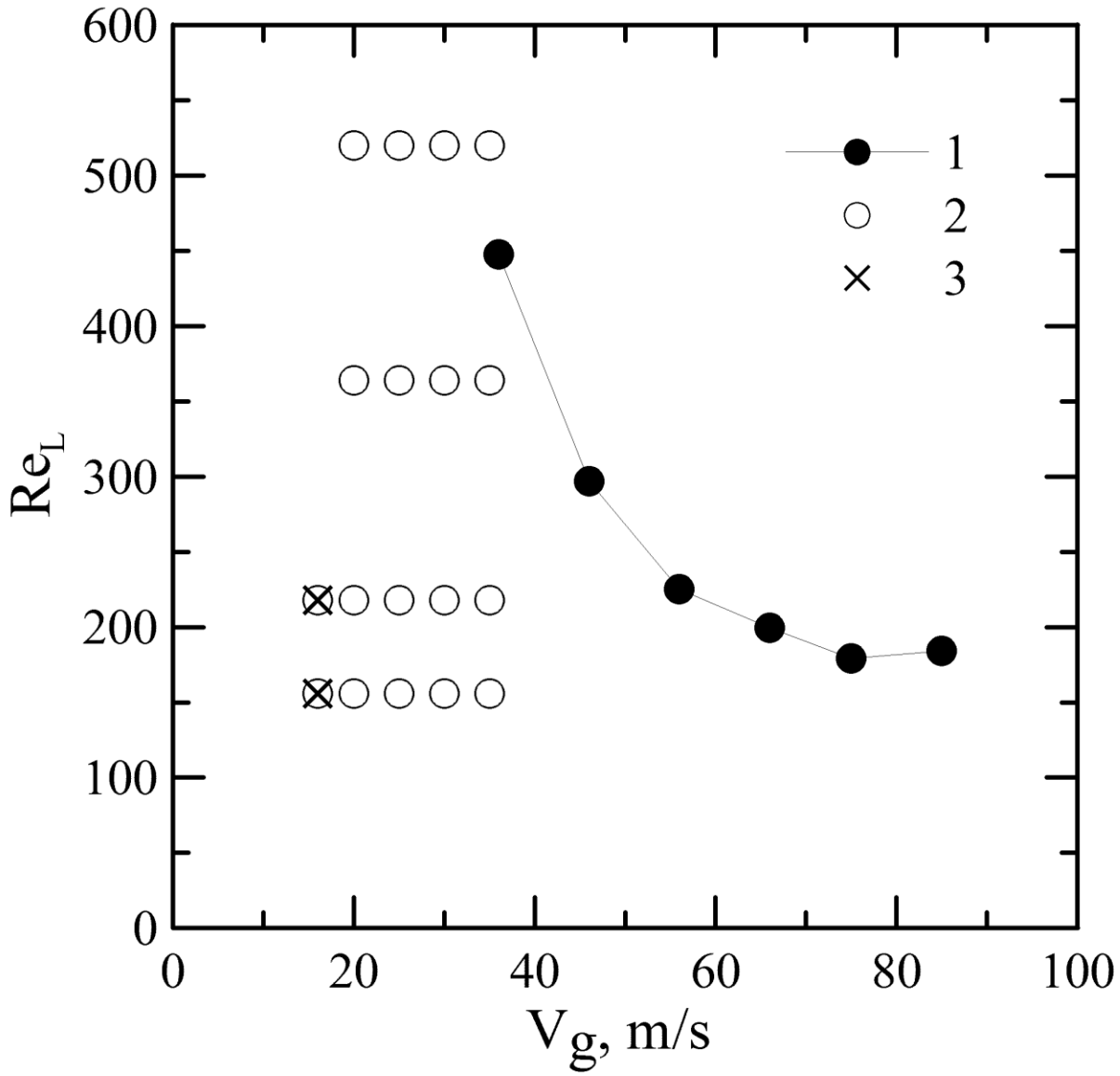

Diagram 12